

The effect of spectral albedo in bifacial photovoltaic performance

Nicholas Riedel-Lyngskær^{a,*}, Martynas Ribaconka^a, Mário Pó^b, Anders Thorseth^a,
Sune Thorsteinsson^a, Carsten Dam-Hansen^a, Michael L. Jakobsen^a

^a Technical University of Denmark, Department of Photonics Engineering, Roskilde, Denmark

^b EKO Instruments B.V., The Hague, the Netherlands

ARTICLE INFO

Keywords:

Spectral albedo
Spectral mismatch
Trackers
Bifacial
Normalized difference vegetation index

ABSTRACT

This paper analyzes 15-months of spectral albedo measurements collected at the Technical University of Denmark (55.6°N, 12.1°E). High-resolution spectroradiometers are used to monitor four albedo scenarios, which include green vegetation, dry vegetation, gravel, and snow. Spectral mismatch and spectral impact are calculated for the front and backside of three different bifacial cell concepts mounted on horizontal single axis trackers and fixed-tilt substructures. The spectral nature of albedo is shown to have significant influence on bifacial photovoltaic performance wherein backside spectral impact as high as 1.20 is observed for fixed-tilt systems above green vegetation and as low as 0.98 for systems above snow. The results reveal that spectral impact is always lower on tracked than fixed-tilt systems because a greater fraction of sky diffuse light reaches the backside of tracked systems. Given the variety of albedos tested here, we find that the normalized difference vegetation index is a good predictor of backside spectral effects. When the high-resolution measurements are truncated to 4 to 8 carefully selected wavelengths, we find that this limited measurement resolution sufficiently captures the seasonal spectral albedo fluctuations that influence bifacial photovoltaic energy production. Finally, to alleviate the dearth of spectral datasets presently available to the PV community, the spectral irradiance and albedo measurements are made freely available in open access format (<https://doi.org/10.11583/DTU.14695437.v1>).

1. Introduction and literature review

In the mid-2010s, the photovoltaic (PV) industry began shifting crystalline-silicon (c-Si) cell production away from aluminum back surface field (Al-BSF) cells toward passivated emitter and rear cell (PERC) technology (Dullweber, et al., 2016); (Dullweber and Schmidt, 2016). The subsequent cost reductions in industrial-scale PERC manufacturing processes paved the way for a revival of bifacial PV cells and modules. Once viewed as a niche technology used in small-scale applications like the sun-shading elements presented in (Hezel, 2003), the noise barriers in (Nordmann, et al., 2012), and the collection of systems displayed in the introduction of (Ledesma, et al., 2020), bifacial PV is now a mainstream technology with over 20 GW deployed worldwide (Kopecek and Libal, 2021). It has been estimated that 70%–90% of PV modules made during the last three decades were produced with Al-BSF cells (Green, 2015); (Wilson, et al., 2020), but this market majority has been quickly replaced by PERC and bifacial PERC cell technology. The 2021 ITRPV report estimates that by 2025 roughly 60% of PV modules produced will contain bifacial cells, and that by this time, the

Al-BSF concept will be phased out (VDMA, 2021).

Recent research has characterized many of the nuanced performance effects present in bifacial PV systems and quantified how bifacial energy gains are influenced by installation and environmental conditions. For example, the backside edge brightening effect and electrical losses induced by nonuniformly distributed irradiance were simulated in detail by (Deline, et al., 2020) and (McIntosh, et al., 2019); the susceptibility to power loss from tracker torque tube shading was first described by Pelaez et al. (2019a) with Radiance based ray trace simulations (Ward, 1994) using the opensource Python library bifacial_radiance (Deline and Pelaez, 2017); other researchers later used bifacial_radiance to investigate similar backside shading effects for system types such as equator-facing static tilts (Berrian and Libal, 2020), (Korevaar, et al., 2020), and two-in-portrait trackers (Riedel-Lyngskær et al., 2020a); electrical mismatch losses induced by nonuniform rear irradiance were investigated experimentally on fixed-tilt systems by (Rossa, et al., 2021) and (Zhang, et al., 2020), and on trackers by (McIntosh, et al., 2020) and (Riedel-Lyngskær et al., 2020a); the dissimilar thermodynamic behavior between monofacial and bifacial PV devices was studied by (Lamers, et al., 2018) and (Wang, et al., 2020); and parametric studies that

* Corresponding author.

E-mail address: nrie@fotonik.dtu.dk (N. Riedel-Lyngskær).

<https://doi.org/10.1016/j.solener.2021.12.023>

Received 13 September 2021; Received in revised form 1 December 2021; Accepted 13 December 2021

Available online 24 December 2021

0038-092X/© 2021 The Authors. Published by Elsevier Ltd on behalf of International Solar Energy Society. This is an open access article under the CC BY license

(<http://creativecommons.org/licenses/by/4.0/>).

Nomenclature			
α	Albedo	FT	Fixed tilt structure
I_{SC}	Short-circuit current	GHI	Global horizontal irradiance
K_d	Diffuse to global horizontal irradiance fraction	G_{POA}	Global irradiance in plane-of-array
Θ_z	Solar zenith angle	HSAT	Horizontal single axis tracker
<i>Subscripts</i>		IBC	Interdigitated back contact
λ	Wavelength resolved data	MBE	Mean bias error
Back	Backside device performance	MFR	Multi-filter radiometer
Front	Front side device performance	NDVI	Normalized difference vegetation index
<i>Abbreviations</i>		NIR	Near infrared (700 – 1000 nm in this work)
Al-BSF	Aluminum back surface field	PERC	Passivated emitter and rear cell
BEG	Bifacial energy gain	PERT	Passivated emitter rear totally diffused
DfHI	Diffuse horizontal irradiance	RHI	Reflected horizontal irradiance
DNI	Direct normal irradiance	SMM	Spectral mismatch factor
FOV	Field of view	SI	Spectral impact
		SR	Spectral responsivity
		VIS	Visible light (400 – 700 nm in this work)

simulated bifacial energy gains due to module orientation, height, row spacing and diffuse light content were presented in (Asgharzadeh, et al., 2018), (Chudinzow, et al., 2020), (Guo, et al., 2013), (Sun, et al., 2018), and (Yusufoglu, et al., 2015).

No less important than these installation and environmental influences is the ground surface albedo. Defined as the percentage of incident sunlight (beam and sky diffuse) that a surface reflects, the albedo determines the amount of ground reflected radiation available for PV energy conversion. Ground reflected radiation constitutes less than 3% of the total effective irradiance for the majority of monofacial systems and can amount to less than 1% of the total irradiance when the tilt angle from horizontal is less than 25°. In contrast, ground reflected radiation contributes approximately 10% of the effective irradiance received by most bifacial systems worldwide (Pelaez et al., 2019a); (Rodriguez-Gallegos, et al., 2020) and (Sun, et al., 2018). Indeed, the rear irradiance received by bifacial systems is increased to some extent by sky diffuse irradiance, and in some conditions, by beam irradiance reaching the backside. However, the contributions of sky diffuse and beam irradiance to the total rear irradiance are either small or negligible compared to ground reflected contributions (Chiodetti, et al., 2016); (Chudinzow et al., 2019).

The albedo of natural and synthetic materials varies with the wavelength of incident sunlight, which is a property referred to as spectral albedo or spectral reflectance. Some of the earliest spectral albedo measurement campaigns were intended to understand the Earth's energy balance (Krinov, 1953), the spectral properties of plants (Gates et al., 1965), water bodies and snow (Kondratiev et al., 1964). Prior to 2016, spectral albedo was sparsely studied within the context of PV applications (Andrews and Pearce, 2013); (Brennan et al., 2014), which is likely because ground reflected radiation contributes minimally to monofacial PV performance. In the wake of ever-increasing bifacial PV deployments, however, there has been a subsequent upswing in the spectral albedo investigations conducted by PV researchers (Blakesley et al., 2020); (Gostein et al., 2020); (Monokroussos et al., 2020); (Pal et al., 2020); (Russel et al., 2017); (Vogt et al., 2018). One common conclusion we found among these studies is that spectral albedo effects can significantly influence the backside irradiance received by PV bifacial systems—up to 30 % in some cases—and that these effects should be accounted for in bifacial PV simulations (Blakesley et al., 2020); (Gostein et al., 2020); (Vogt et al., 2018). Several works have accordingly incorporated spectral albedo into bifacial PV performance models. All such studies use spectral albedo data from the ASTER spectral library (Baldrige et al., 2009) and the implicit assumption that the distribution of the spectral albedo does not change with time and

conditions (Dupre et al., 2020) (McIntosh et al., 2019); (Mekemeche and Beghdad, 2020); (Russel et al., 2017); (Tuomiranta et al., 2020); (Ziar et al., 2019).

To our knowledge, the literature is lacking in contributions where diurnal and seasonal spectral albedo shifts are analyzed within the context of bifacial PV performance. The only work that we are aware of covering this topic is (Blakesley et al., 2020), who calculated spectrally effective albedo for three bifacial PV device types using satellite and ground-based spectral albedo measurements in Namibia and France. The present contribution reports on continuous high spectral resolution albedo measurements made in Roskilde, Denmark (55.6° N, 12.1° E) over a 15-month period. The objectives are to demonstrate how temporal changes in spectral albedo affect the performance of commercially available bifacial PV devices mounted in different orientations, and to provide recommendations for how field measurements can be used to account for spectral albedo shifts that affect bifacial energy output.

2. Methodology

2.1. On site measurements

Spectral irradiance data in the range of 300 – 1100 nm were recorded every 5 min by three EKO MS-711 spectroradiometers. The Si detector inside each spectroradiometer contains 2048 pixels, which provides a wavelength scale with 0.4 nm sampling interval. The optical resolution (full-width half maximum) of the instruments is 7 nm. Two of the spectroradiometers have a 180° field-of-view (FOV) and were horizontally mounted on a measurement stand 1.5 m above the ground (Fig. 1). The upward facing spectroradiometer recorded the global horizontal spectral irradiance (GHI_λ) and the downward facing instrument recorded the ground reflected horizontal spectral irradiance (RHI_λ). The spectral albedo α_λ was calculated according to Eq. (1).

$$\alpha(\lambda) = \frac{RHI(\lambda)}{GHI(\lambda)} \quad (1)$$

The third spectroradiometer has a 5° FOV collimation tube and was mounted on a dual-axis tracker to measure the direct normal spectral irradiance DNI_λ . This is the same instrument used in (Riedel et al., 2018) and is installed nearby in a 15 m tower where horizon shading is negligible. The diffuse horizontal spectral irradiance $DfHI_\lambda$ was calculated from the difference between the measured GHI_λ and the measured DNI_λ adjusted by the zenith angle (θ_z) according to Lambert's cosine law.

$$DfHI(\lambda) = GHI(\lambda) - DNI(\lambda) \cdot \cos\theta_z \quad (2)$$

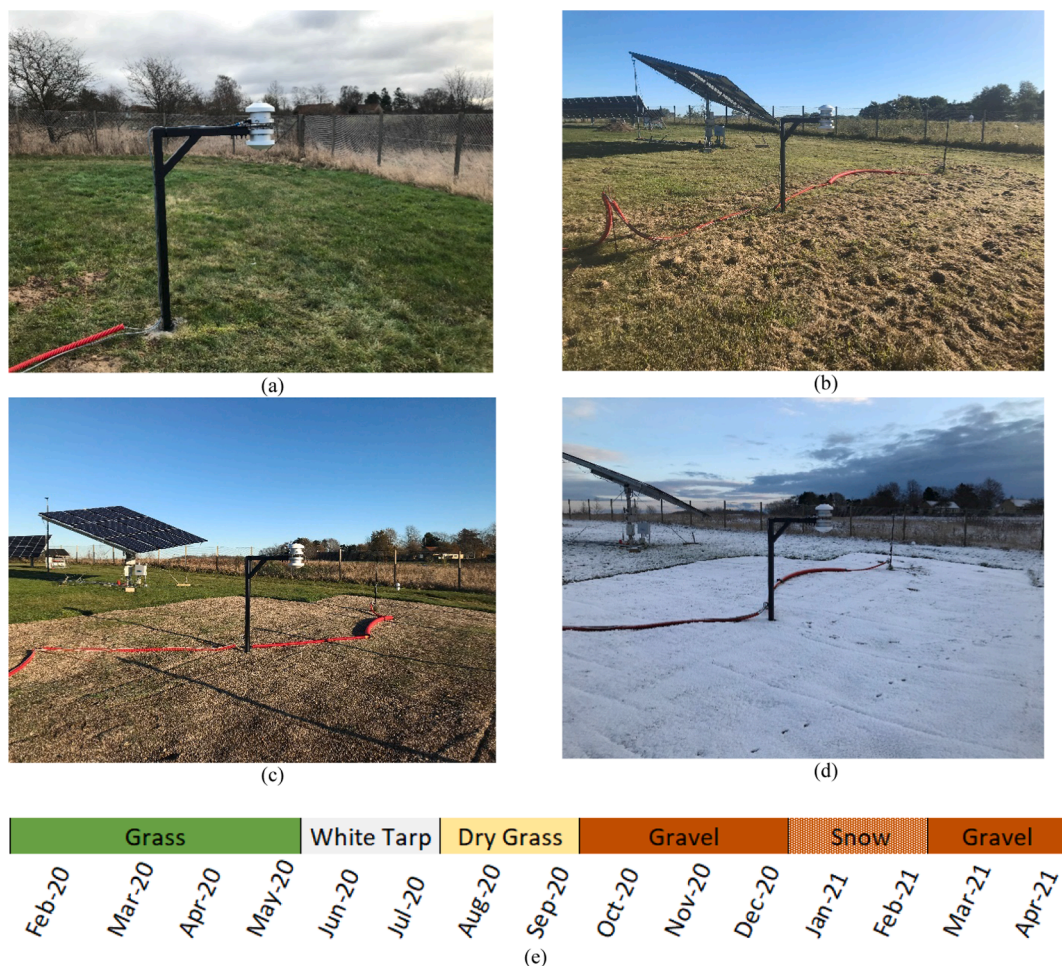


Fig. 1. Spectral albedo measurement stand and the various albedo conditions tested at Technical University of Denmark: (a) Green grass from February to May 2020, (b) dry grass from August to September 2020, (c) 5 – 8 mm gravel from September 2020 to April 2021, (d) snow in January 2021, and (e) timeline of the ground surfaces tested during the campaign. (For interpretation of the references to colour in this figure legend, the reader is referred to the web version of this article.)

The field measurement campaign investigated the diurnal and seasonal variations in spectral albedo under four surfaces/conditions including green grass (Fig. 1a), dry grass (Fig. 1b), gravel (Fig. 1c), and snow (Fig. 1d). A timeline is shown in Fig. 1e. The spectral RHI_λ , GHI_λ and DNI_λ data, as well as the weather data and broadband albedo data recorded during this period are available to the solar energy community in an open access format (<https://doi.org/10.11583/DTU.14695437.v1>).

Healthy green grass was measured for three months from 05.02.2020 to 06.05.2020. From 07.05.2020 to 27.07.2020 a highly reflective white tarp was affixed to the ground with the spectral albedo stand in the center. The data recorded during the white tarp period are not reported here because the white tarp’s area was not large enough to limit the light reflected off the surrounding grass to less than 5% of the total signal received by the downward facing spectroradiometer. However, the spectral albedo measurements from the white tarp albedo period are available in the open access dataset.

The grass began to dry out shortly after the white tarp was removed (Fig. 1b). The period of dry grass albedo measurements spanned from 28.07.2020 to 07.09.2020. On 08.09.2020, a 12 m by 12 m gravel mixture (consisting of 5 – 8 mm diameter stones) was distributed in an area covering the majority of the spectroradiometer’s FOV and remained in place until the measurement campaign concluded on 29.04.2021 (Fig. 1c). We estimate that more than 97% of the ground reflected light reaching the downward facing instrument originates from the 144 m² gravel area. Periodic snowfall occurred in winter 2021 (Fig. 1d) and was

recorded by a Lufft UMB600 weather sensor. There were five days when the daily snowfall was greater than 25 mm. Onsite snow depth data are not available, but snowfall hardly accumulates in Denmark’s predominantly humid continental climate (Köppen climate classification Dfb), and the snowfall that we observed melted completely within a day or two.

The albedo measurements reported here are not split into black-sky and white-sky albedo components, but the open access data set allows users to perform such a decomposition if desired. The black-sky and white-sky albedos can be determined with the procedure described by (Michalsky and Hodges, 2013). This method requires measurements from a clear sky day and a cloudy day with the criterion that ground conditions do not change appreciably between the clear sky and cloudy period.

The upward and downward facing spectroradiometers shown in Fig. 1 did not acquire measurements simultaneously because a single datalogger was used to acquire data from both instruments. We observed delays of up to 10–15 s between the time at which the first spectroradiometer began its measurement, to when the second unit completed its measurement. This delay is due to data processing time in the logger and the exposure times in each sensor, which take 10 to 5000 ms each, depending on the light intensity. An irradiance stability check was used because Eq. (1) assumes a constant condition during the GHI_λ and RHI_λ measurements. Broadband GHI data recorded every 10 s were used to calculate a variability index (VI) (Stein et al., 2012) within a 2-minute period: approximately 1 min before and after the spectral albedo

measurement. Measurements were removed from the analysis when the VI was greater than 1.1, which served as an irradiance stability filter. Data recorded on detector edges (λ less than 300 nm and λ greater than 1050 nm) were also removed because as these data are prone to measurement noise.

Typically, the spectral sensitivity of Si spectroradiometers is between 300 and 1100 nm, which makes analysis of Si PV devices challenging because the spectral responsivity of contemporary Si PV (e.g., PERC) is between 300 and 1200 nm (Belluardo et al., 2018). Since the useful spectral range is 300 to 1050 nm, and the bifacial devices we analyzed are spectrally responsive between 300 and 1200 nm (Fig. 3), we used the SMARTS model (Gueymard, 1995) to fill the spectral irradiance gap between 1050 and 1200 nm. We used the real-time solar zenith angle as a proxy for air mass, the ambient temperature, and atmospheric pressure to generate a SMARTS clear sky spectrum for each spectral measurement. The simulated clear sky spectra were scaled with the cloud opacity factor of (Ernst et al., 2016), which was calculated with broadband global and diffuse irradiance from two onsite pyranometers. However, we have found that the stochastic nature of cloud cover is nearly impossible to account for with a single cloud coverage factor and therefore, the simulated spectra from 1050 to 1200 nm were scaled with a secondary factor to ensure that the simulated spectra align with the measurements at 1050 nm. It is worth noting that under the AM1.5G reference spectrum (International Electrotechnical Commission, 2019a), the bifacial PV devices we analyzed (Fig. 3) generate approximately 4% of their total photocurrent from light between 1050 and 1200 nm. Therefore, the extension imposes a small effect on the results reported here.

2.2. Spectroradiometer calibration

Calibration of all three spectroradiometers was performed inhouse at DTU Fotonik's DOLL laboratories on 22.01.2020, two weeks before the field measurement campaign began. The calibration setup consists of a NIST traceable Optronics Laboratories FEL-type lamp that is calibrated for spectral irradiance and placed on an alignment jig 50 cm from the device under test with measures to mitigate stray light. The spectral responsivity is calculated as the certified spectral irradiance of the lamp divided by the spectral pixel count and multiplied by the integration time used during calibration. The expanded uncertainty of the calibration is approximately 4.5% for wavelengths between 400 and 1050 nm, but between 300 and 400 nm, the uncertainty can be as high as 10% (Fig. 2a). The primary uncertainty contributions in the setup are the lamp drift (4.0%), and the low signal to noise ratios at the extreme ends of the spectroradiometer sensitivity.

A final measurement of the standard lamp was made on 11.05.2021 to check the spectroradiometers for any drift that occurred during the measurement campaign. The lamp is stored and operated in ways that minimize changes in output, the electrical power applied to the lamp is precisely monitored during calibrations, and the lamp is periodically compared to other in-house reference lamps to detect any drift. Fig. 2b shows each spectroradiometer's measured deviations to the standard lamp spectrum upon completion of the 15-month measurement campaign, and highlights that the magnitude of the measurement drift is dependent on the instrument and wavelength. (Dirnberger et al., 2015a) showed that a comparable spectroradiometer deployed in Freiburg, Germany for two years had less than $\pm 5\%$ drift between 400 and 1100 nm – a magnitude that is comparable to the DNI and GHI instrument drifts shown in Fig. 2b.

The spectroradiometer used for RHI measurements showed the highest deviations to the reference lamp (mean deviation to reference lamp of $+3.3\%$, 95% of measurements within $\pm 5.6\%$) and showed pronounced kinks at certain wavelengths (e.g., 645 nm and 670 nm). The most pronounced kinks overlap with sharp gradients in the spectral responsivity of the instrument. This means that small changes in the wavelength response will be amplified near the wavelength where these

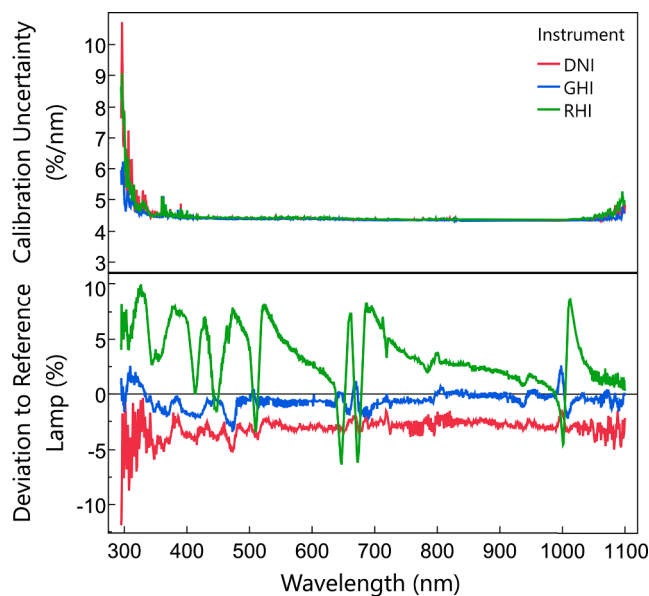


Fig. 2. (a) Uncertainty ($k = 2$) of the calibration check performed on 11.05.2021, two weeks after completion of the measurement campaign. (b) Measured deviations to the FEL-type reference lamp after 15 consecutive months of field operation. The averages of ten measurements made with each instrument are shown.

gradients reside. The results from the calibration events on 22.01.2020 and 11.05.2021 suggest that the spectral responsivity of the RHI instrument was affected during the outdoor experiments. In Section 3.3 we describe the extent to which the kinks observed in the RHI instrument affected spectral mismatch calculations.

An expanded uncertainty estimation of the continuous outdoor solar spectral irradiance measurements would be a complex task in of its own. Monte-Carlo approaches are commonly used to account for the correlation between spectroradiometer uncertainty components and wavelength (Dirnberger et al., 2015a), (Hohl-Ebinger and Warta, 2011), (Schinke et al., 2020), but the time-dependency of continuous solar spectral measurements introduces additional constraints and complexity that can limit the applicability of the Monte Carlo method. Although expanded uncertainty has not been made for the continuous outdoor measurements performed in this work, the instruments have participated in international laboratory intercomparisons in 2017 (Pravettoni et al., 2018) and 2018 (Galleano et al., 2019) to establish confidence in the calibration and measurement accuracy. The angular response of the horizontally mounted EKO MS-711 spectroradiometers follow a cosine response within 3% or better. This cosine error will primarily affect the upward facing (GHI) instrument at high solar zenith angles in direct sunlight. Finally, all three spectroradiometers contain thermoelectric heating and cooling, which maintained detector temperatures of $25 \text{ }^\circ\text{C} \pm 0.5^\circ$ during approximately 98% of the field measurements.

2.3. Bifacial cell technologies

Fig. 3 shows the front and backside spectral responsivities of the bifacial cells studied. The cell concepts include interdigitated back contact (IBC), n-type passivated emitter and rear totally diffused (n-PERT), and p-type passivated emitter and rear cell (PERC). These were chosen for their varying rear to frontside efficiencies (i.e., bifaciality factors) and availability. Under AM1.5G illumination, the bifaciality factors of the IBC, n-PERT and PERC cells are 62%, 88% and 75%, respectively. Note that bifaciality factors of full-size modules will be lower than on a cell-level because the active backside of modules is commonly shadowed by junction boxes, labels, frames, and/or a glazing printed on the glass between cell spacings.

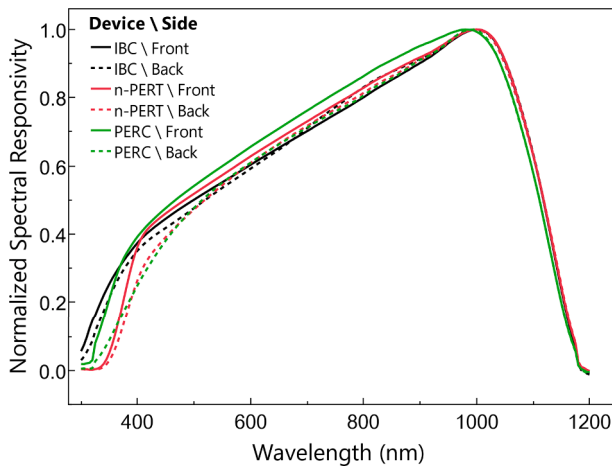


Fig. 3. Normalized spectral responsivity of the three bifacial cell types studied. The cells are encapsulated in standard PV glass.

The spectral responsivity measurements shown in Fig. 3 are of single cells laminated inside 20 × 20 cm PV glass. The measurements were performed with a PV Measurements QEXL quantum efficiency measurement system. The bifacial IBC device is the ZEBRA cell with front surface field (FSF) emitter developed at ISC Konstanz (Kopecek et al., 2020). The bifacial n-PERT device is the BiSoN (bifacial on n-type) concept, also produced by ISC Konstanz (Lossen et al., 2015). The PERC cell was procured from Blue Sun Solar.

2.4. Optical modeling

Most bifacial PV systems are mounted at non-horizontal tilt angles, which allows light from the sky hemisphere to reach the backside. Since sky diffuse light can have a markedly different spectral distribution than the albedo, a thorough study of spectral effects in bifacial systems requires data in the rear plane-of-array (POA). We used the 2D view factor model pvfactors (Anoma et al., 2017) to calculate global frontside and rear POA spectral irradiances ($G_{POA,Front,\lambda}$ and $G_{POA,Rear,\lambda}$). View factors are used in radiative heat transfer theory to describe the fraction of radiation emitted from surface A that strikes surface B, expressed as $F_{A \rightarrow B}$. We selected pvfactors as the engine for 2D view factor modeling due to its open-source nature and because it showed good agreement to broadband $G_{POA,Rear}$ measurements in our previous work (Riedel-Lyngskær et al., 2020b). We performed simulations for two orientations: a 25° south facing fixed-tilt (FT) system and a horizontal single-axis tracking (HSAT) system. These two system types were chosen because they are commonly implemented in large-scale PV systems and are the same configuration as the bifacial PERC systems collocated at the measurement site.

Table 1 summarizes the structural details of the FT and HSAT systems simulated, which correspond to the real 45 m long bifacial PV arrays that are installed onsite. Five-rows of FT and HSAT systems are simulated, and all results reported here are from the center row. The 2D view factor method assumes that rows are infinitely long and thereby

Table 1
Structural specifications of the two-in-portrait PV systems simulated in this work.

Specification	Fixed-Tilt	Single Axis Tracker
Tilt Angle from horizontal (°)	25	± 60
Surface azimuth (°)	180	90 or 270
Ground clearance* / Hub height (m)	0.9	2.0
Ground cover ratio	0.40	0.28

*Ground clearance corresponds to the fixed-tilt system while hub height corresponds to the tracker.

neglects edge brightening effects, but the works of Berrian (2020) and Pelaez et al. (2019b) have shown that the performance of the center array within a five-row system, at least 10 m long, is comparable to the performance of an array within a semi-infinite field. In other words, five rows can accurately represent utility-scale installations.

The measured (α_s, DNI_s) and calculated ($DfHI_s$) spectral data were passed to the 2D view factor model (pvfactors), one wavelength at a time in 1 nm steps from 300 to 1200 nm. The full simulation mode of the model was used to calculate the spectral radiosity of all surfaces within the modeled scene for each respective wavelength λ . Angular reflection losses at the front and rear module surface are accounted for with the Sandia incident angle modifier (IAM) model (King et al., 2004). An IAM profile for a c-Si module with non-antireflective coated glass was used for the rear side.

2.5. Data analysis

The large volume of data recorded by high-resolution spectral instruments in continuous operation can be challenging to analyze – especially over multi-year timescales. Qualitative metrics such as the average photon energy parameter (Dirnberger et al., 2015)b, (Nofuentes et al., 2017) are useful in this respect because they permit a quick and simple analysis of spectral shifts within a vast dataset that potentially contains several 100 million records, or more. To this end, we used the normalized difference vegetation index (NDVI) to identify significant changes in the spectral albedo distribution during the 15-month campaign. First proposed by (Rouse et al., 1974), the NDVI is commonly used in remote sensing to identify vegetated areas from satellite images. The NDVI is a dimensionless quantity on a scale of -1 to +1 and is calculated according to Eq. (3).

$$NDVI = \frac{NIR - VIS}{NIR + VIS} \tag{3}$$

In this work, the VIS and NIR quantities are the integral of the spectral RHI from 400–700 nm and 700–1000 nm, respectively. The concept behind NDVI is that healthy green vegetation reflects very little visible light (VIS) but reflects significantly in the near infrared (NIR) region. Thus, green vegetation has a large difference between NIR and VIS reflectance and has a high positive NDVI value. As vegetation goes through drying stages of senescence to death, it continuously loses chlorophyll, which results in increased VIS reflection and a smaller difference between NIR and VIS. During snow albedo conditions, the NDVI is near zero or slightly negative (Dye and Tucker, 2003).

The spectral POA irradiance $G_{POA,Front,\lambda}$ and $G_{POA,Rear,\lambda}$ were summarized using the spectral mismatch factor (SMM) per Equation 7 in IEC 60904-7 (International Electrotechnical Commission, 2019b). We introduce subscript j to denote the front or rear side of the PV device and POA.

$$SMM_j = \frac{G_{Ref} \cdot \int_a^b SR_j(\lambda) \cdot G_{POA,j}(\lambda) d\lambda}{G_{POA,j} \cdot \int_a^b SR_j(\lambda) \cdot G_{Ref}(\lambda) d\lambda} \tag{4}$$

SR_{Front} and SR_{Back} are the front and backside spectral responsivity, and $G_{Ref,\lambda}$ is the AM1.5G reference spectrum defined in IEC 60904-3 (International Electrotechnical Commission, 2019a). The integration limits a to b are 300 to 1200 nm. As pyranometer data in the POA were not available for each albedo scenario (Fig. 1), $G_{POA,j}$ is calculated as the integral of $G_{POA,Front,\lambda}$ or $G_{POA,Rear,\lambda}$, and G_{Ref} is calculated as the integral of $G_{Ref,\lambda}$ over the same integration limits. SMM_{Back} was calculated for the three types of bifacial PV cell concepts shown in Fig. 3.

Eq. (4) is simply the ratio of two ratios. The numerator is the short-circuit current (I_{SC}) under the observed spectral condition $G_{POA,j,\lambda}$, divided by the broadband irradiance $G_{POA,rear}$, and the denominator is the I_{SC} under the AM1.5G reference spectrum $G_{Ref,\lambda}$ divided by the broadband irradiance G_{Ref} . SMM values greater than 1 thus indicate spectrally induced gains in I_{SC} relative to AM1.5G, and SMM values less

than 1 indicate spectrally induced I_{SC} losses. When analyzing temporal spectral shifts over time, it is typical to report the so-called the ‘spectral impact’ or ‘spectral effect’, which is the SMM weighted by broadband POA irradiance during a given period (Alonso-Abella et al., 2014), (Dirnberger et al., 2015b), (Pelland et al., 2020) (Polo et al., 2017). Following this practice, spectral impact (SI) was calculated for the front and backsides according to Eq. (5).

$$SI_j = \frac{\sum SMM_j \cdot G_{POA,j}}{\sum G_{POA,j}} \quad (5)$$

3. Results and discussion

3.1. Diurnal spectral albedo trends

Albedo measurements on clear days show a strong dependency on solar zenith angle (Θ_z), while albedo measurements remain reasonably constant on cloudy days without precipitation (Coakley, 2003) (Vignola et al., 2017). Fig. 4 shows normalized spectral albedo on selected clear and cloudy days at 100 nm resolution. The data are normalized to the spectral albedo observed at solar noon (180° solar azimuth). These plots are intended to reveal some of the nuanced spectral albedo effects that are embedded in the SMM summary presented in Section 3.3.

The daily horizontal diffuse to global fraction (K_d) on the clear days was less than 0.40, while on cloudy days K_d was greater than 0.95. Albedo increases with decreases in sun height on clear days, but only down to solar elevation angles of about 10° at which point the albedo decreases (Iqbal, 1983). This phenomenon occurs because the fraction of horizontal diffuse to horizontal beam irradiance rapidly increases as the solar elevation angle decreases from 10° toward the horizon. Therefore, we only show measurements when the sun is higher than 10° above the horizon in Fig. 4a, Fig. 4c, and Fig. 4e.

Increases in albedo with solar zenith angle are a familiar characteristic found in broadband albedo observations on clear days (Dittmann et al., 2019), (Marion, 2021). In the case of spectral albedo measurements, however, the solar zenith dependency is not equal across all wavelengths. The tendency shown here is for near infrared (NIR) wavelengths to show greater solar zenith dependency than visible (VIS) or UV wavelengths, which is consistent with measurements reported by

(Kondratyev, 1969), (Michalsky and Hodges, 2013). Fig. 4a, Fig. 4c and Fig. 4e show that albedo tends to be higher after solar noon than before solar noon. Other authors have reported such asymmetrical daily trends for spectral albedo (Kondratyev, 1969), (Michalsky and Hodges, 2013) and broadband albedo (Chiodetti et al., 2016) (Minnis et al., 1997) (Stueve, 2019). Since instrument leveling checks were regularly performed, we attribute the asymmetry shown here to the mostly western grade in the albedo stand vicinity ($\max 4^\circ$). The slight westerly slope results in greater ground illumination—and thus reflectance—in the afternoon than in the morning.

The clear sky green grass albedo data recorded on 21.04.2020 (Fig. 4a) show a pronounced dip in the early morning that returned to expected albedo levels once the sun elevation reached about 20° . Shadows cast from objects in the horizon have been ruled out for several reasons: the GHI_λ measurements were unaffected during the albedo dip, our measured skyline profile indicated that there should be no eastern shading when the sun elevation is above 5° , and the gravel albedo data recorded 364 days later—during nearly identical solar angles—showed no such morning dip. The cause for the dip is still uncertain but is presently attributed to possible morning dew formed on the grass, which evaporated as broadband DNI became sufficiently high and relative humidity sufficiently low.

Fig. 4b and Fig. 4f show examples when the cloudy day albedo is not constant. In Fig. 4b, a rainfall event caused a small, but noticeable, wavelength-dependent decrease in grass albedo. During the cloudy day gravel albedo measurements (Fig. 4f), two light snowfall events caused a 50% increase in albedo (e.g., 0.2 to 0.3 at 950 nm). This is roughly consistent with (Marion, 2021) who reported melting snow albedos of 0.4 or less. Note that the thermoelectric elements inside the spectroradiometers maintain the detector temperature at $25^\circ\text{C} \pm 0.5^\circ\text{C}$, which melts snow deposited on the instruments. However, water droplets from rain and melted snow could affect the measurements during precipitation.

3.2. Seasonal spectral albedo trends

The NDVI is frequently used in remote sensing applications to assess the spectral reflectance of Earth’s surface (Huang et al., 2020), but as far

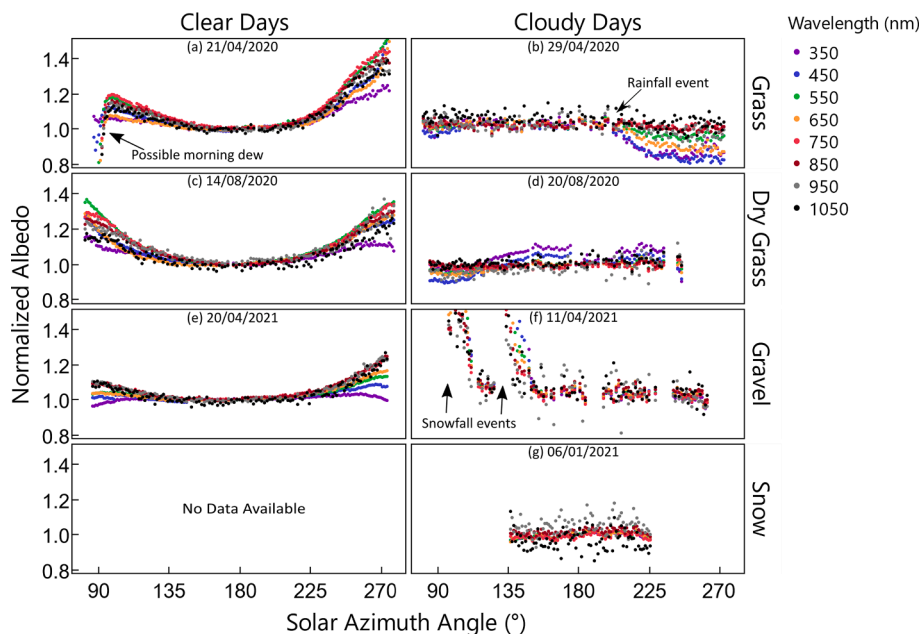


Fig. 4. Spectral albedo for select wavelengths normalized to the albedo observed at solar noon. Figures in the lefthand column contain data recorded during clear sky conditions and figures in the righthand column contain data recorded on cloudy days. The four rows indicate the state of the ground cover during measurement: Green grass, dry grass, gravel and snow. (For interpretation of the references to colour in this figure legend, the reader is referred to the web version of this article.)

as we are aware, the NDVI metric has not yet been applied to bifacial PV applications. Fig. 5 shows the NDVI values observed during the 8-month grass period, excluding the two months when the white tarp was affixed to the ground. The results are typical of seasonal vegetation with maximum NDVIs of approximately 0.7 (green vegetation) and minimum NDVIs of approximately 0.1 (dry vegetation). The NDVI was reasonably stable between 0.6 and 0.7 for the first 3.5 months of the measurement campaign and a rapid decrease in NDVI occurred in summer 2020 when the grass was quickly drying. If the spectral albedo measurements of grass had continued for another year or more, we expect that NDVI would have recovered to approximately 0.6 and followed a cyclical pattern each year, likely with the lowest NDVIs in summer.

The vertical green line and yellow line in Fig. 5 indicate the highest and lowest NDVI values observed on clear days. Fig. 6 displays the albedo measurements on these days and reveals the most extreme seasonal variations recorded. The largest differences between the green grass and dry grass albedo are in the visible light region (400–700 nm). The reflectance and absorption of light in this region is determined by the amount of chlorophyll in the grass: The green grass albedo (Fig. 5a) shows low reflection and high absorption of visible light, while the dry grass albedo (Fig. 5b) shows higher reflection and lower absorption.

Our previous work (Riedel-Lyngskær et al., 2021) showed that spectral albedo curves from databases (e.g., that of (Baldrige et al., 2009)) often fail to agree with the measured albedo curves' shape and magnitude across all wavelengths and days. This observation suggests that information such as genus, species, water content and growth state is likely required to select spectral albedo data that is representative of a given site. The significant shift toward NIR wavelengths in green grass's albedo (Fig. 6a) presents an important implication for its measurement with broadband sensors. Specifically, our previous work (Riedel-Lyngskær et al., 2021) showed that bifacial energy gain calculations can be as much as 3% higher when albedo measurements of vegetation are made with Si devices rather than thermopile pyranometers. Finally, the spectral albedo of vegetation (with open access measurements provided in this work) have significance for the up-and-coming field of agricultural PV, where installations often feature vertically mounted bifacial modules such as those simulated in (Chudinow et al., 2020) and (Robledo et al., 2021). In such vertically mounted PV systems, the ground reflected irradiance can represent a significant percentage of the total in-plane irradiance.

Fig. 7 shows the NDVI values observed during the 7-month gravel period. The NDVIs recorded during snowfall events are indicated with

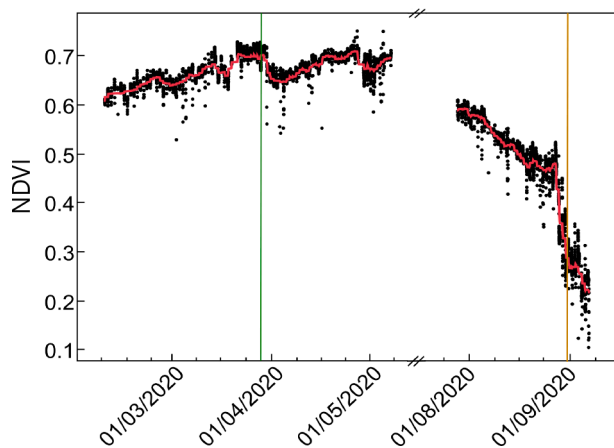


Fig. 5. NDVI from February to September 2020 over grass. The black dots show NDVI measured every five minutes, and the red line shows the one-day rolling average. The vertical green and yellow reference lines indicate the highest and lowest NDVI values recorded on clear days. The spectral albedo recorded on these two days is shown in Fig. 6. (For interpretation of the references to colour in this figure legend, the reader is referred to the web version of this article.)

green markers. The NDVI is mostly between -0.15 and 0.10 when snow is not present, but on days when the gravel was fully covered in snow, the NDVI was as low as -0.3 . The lowest NDVI values in Fig. 7 correspond well to those reported by (Dye and Tucker, 2003) for fully snow-covered areas.

In Fig. 7, the vertical brown reference line indicates a clear day at the beginning of the gravel albedo period, and the blue reference line indicates one of the most severe snowfall days during the test period. Fig. 8 zooms in to the spectral albedo measurements recorded on these two days. Based on local weather measurements, we estimate that the snow depth during the measurements in Fig. 8b was less than 5 cm, that the snow fell within 24 h of measurement, and that the gravel below was completely covered by snow. Although our test site contains various PV module designs that include bifacial, monofacial, framed, and frameless constructions, we did not receive sufficient snowfall to draw meaningful conclusions about their different snow shedding behaviors. But interestingly, recent literature suggests that bifacial modules in certain configurations can offer improved snow shedding performance over monofacial counterparts. (Burnham et al., 2019) conducted side-by-side tests of bifacial and monofacial systems on dual-axis trackers in Burlington, Vermont (44.5°N) and noted that the bifacial systems tended to shed snow faster than monofacial, which they proffered was because the $G_{\text{POA, Rear}}$ exposure caused greater heating of the bifacial arrays. (Riley et al., 2019) observed that the absence of a module frame tends to expedite snow shedding, so long as snow drifts did not accumulate below the array. This phenomenon stands to benefit bifacial systems because they are typically laminated in glass-glass packages, which thereby offers the possibility of frameless construction.

The gravel and snow spectral albedo curves appear smoother than those of vegetation because they do not show the step increase at 700 nm. The smooth shape of the gravel and snow spectral albedos reveal kinks in the measurements (e.g., at 675 nm and 1000 nm) which are artifacts that were not present after the initial calibration on 22.01.2020. A cubic spline fit was applied to obscure the kinks of the binned spectral albedo curves in Fig. 6 and Fig. 8. The fact that these kinks occurred after less than 1 year of deployment demonstrates how sensitive the alignment of the internal optical bench (i.e., mirrors and grating) is to field conditions and highlights the need for regular calibration.

3.3. Spectral mismatch and spectral impact

This section details how the spectral albedo conditions measured at the site impact bifacial PV performance. Fig. 9 shows linear regressions of the daily backside spectral impact (SI_{Back}) versus the daily average NDVI for three bifacial cell concepts and two structures. The datapoints are mostly in two clusters: one for the gravel period without snow, and one for the green grass period. The lowest and highest NDVI values correspond to full snow coverage (-0.3) and green grass (0.7), respectively. The points between the two clusters correspond to the dry grass period in summer.

The shaded areas around the regression lines show the 95% confidence region of the prediction equation, which is about ± 0.04 . The prediction equations for the three bifacial cells in Fig. 9 show negligible differences within the same structure type (e.g., tracking or fixed-tilt). The small differences likely arise because all three cell concepts are based on Si and have the same bandgap. This suggests that a single prediction equation would be suitable for all bifacial cell concepts with Si substrates.

The strong correlation between SMM and NDVI ($R^2 = 0.90\text{--}0.95$) suggests that by measuring albedo with just two spectrally sensitive sensors—one covering the VIS and one covering the NIR—it is possible to reasonably quantify seasonal shifts in backside irradiance relative to the AM1.5G rating. This correlation is potentially advantageous for bifacial system planners because satellite networks make NDVI products available with global coverage (European Space Agency, 2021) (NASA,

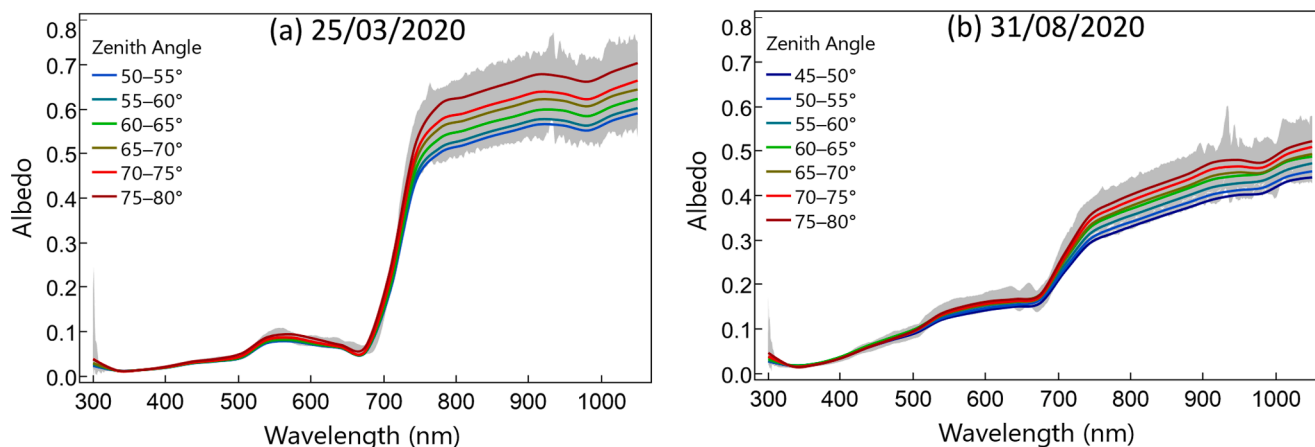


Fig. 6. Spectral albedo measurements on clear days above green grass a) and dry grass b). The solar zenith angle dependency is shown by averaging the spectral albedo data within 5° solar zenith bins. The gray shaded areas represent the range of spectral albedo measurements made on each day. (For interpretation of the references to colour in this figure legend, the reader is referred to the web version of this article.)

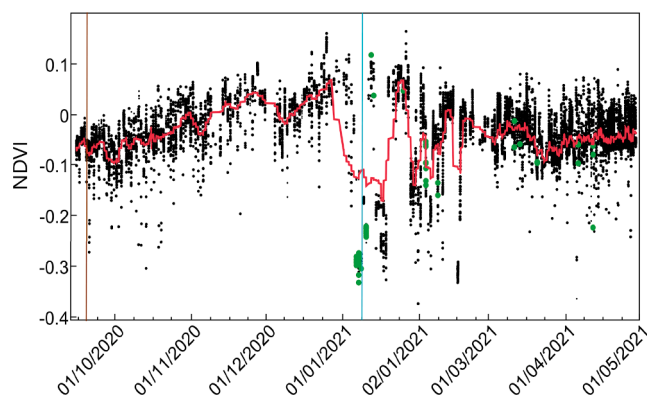


Fig. 7. NDVI from September 2020 to May 2021 over gravel. The black dots show NDVI at 5-minute resolution and the red line shows the one-day rolling average. Green dots indicate the NDVI when snowfall was recorded. (For interpretation of the references to colour in this figure legend, the reader is referred to the web version of this article.)

2021). Although current results indicate that satellite derived NDVI products may be sufficient for estimating seasonal backside POA spectral shifts within about ± 0.04 accuracy, further research is necessary to validate this and to better understand the associated uncertainties.

Table 2 summarizes SI_{Back} on the FT and HSAT systems during the four measured albedo periods. The results for the three cell concepts are

averaged because there is little difference among them. We focus on the backside spectral results in this work because spectral shifts of monofacial Si have been reported for static tilt systems in several locations (Alonso-Abella et al., 2014), (Dirnberger et al., 2015b), (Ishii et al., 2013), (Jessen et al 2018), (Polo et al. 2017) and recently for HSATs in the United States (Ripalda et al., 2020). Nonetheless, a brief statement on our observations of SI_{Front} can be made, which is that SI_{Front} is between 0.983 and 1.017 for the three bifacial cells, two structures, and four albedo conditions studied here. These values are consistent with those reported by other authors.

During clear skies, the output of c-Si devices that are calibrated under AM1.5G will increase with air mass, or as the sun’s spectral distribution shifts toward NIR wavelengths (King et al., 2004) (Myers, 2011). Since the spectral albedos of green grass, dry grass and gravel increase with wavelength (Fig. 6 and Fig. 8), it is reasonable to expect that the bifacial devices studied here will experience spectrally induced gains in I_{SC} when illuminated with these albedo spectra. The results in Table 2 confirm this because SI_{Back} is always greater than 1 for green grass, dry grass, and gravel albedo. Larger spectral albedo shifts toward NIR wavelengths result in greater SI_{Back} values, which is also demonstrated in the correlations of Fig. 9.

The 25° FT system shows higher SI_{Back} values than the HSAT system except during the brief snow albedo period. The differences in SI_{Back} on the two structure types are explained by the different amounts of sky diffuse and ground reflected light received at the backside POA. The backside of the 25° FT system has a constant sky view factor ($F_{Sky \rightarrow PV, Rear}$) of 0.03, meaning that regardless of sun position, 3% of the diffuse

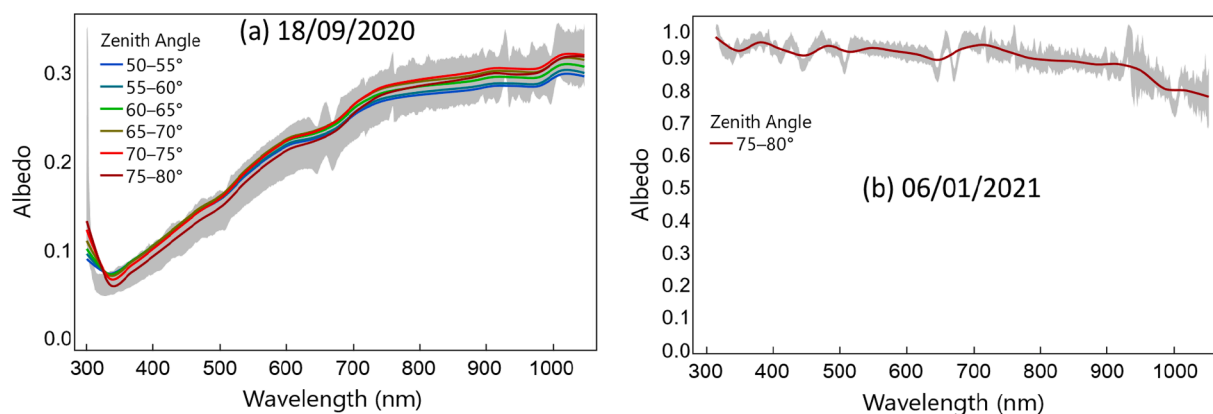


Fig. 8. Spectral albedo measurements of gravel on a clear day a) and of snow on a cloudy day b). The solar zenith angle dependency is shown by averaging the spectral albedo data within 5° solar zenith bins. The gray shaded areas show the range of spectral albedo measurements made on each day.

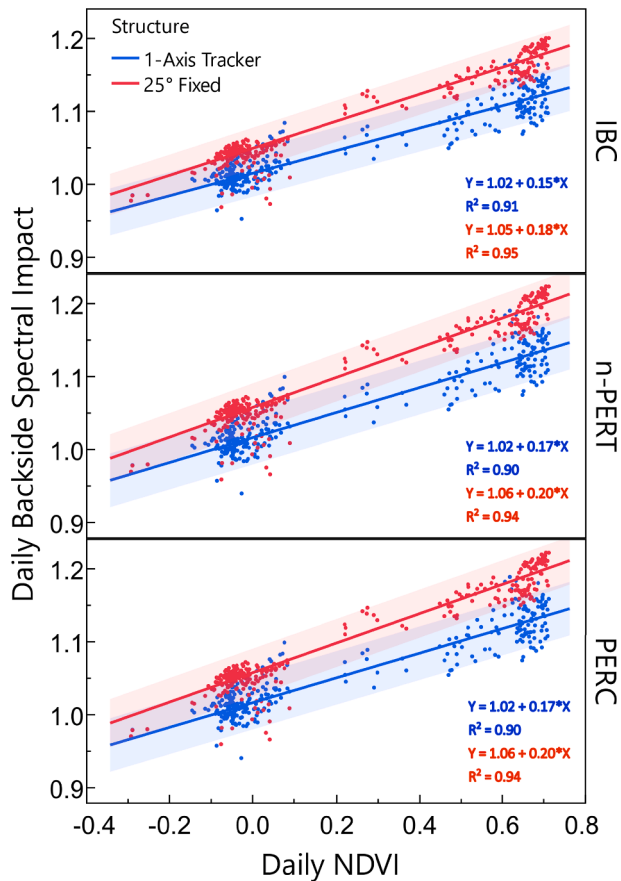


Fig. 9. Correlations of the daily backside spectral impact and normalized difference vegetation index for three bifacial technologies and two structure types. Approximately 15 months of measurements are shown.

light available from the sky hemisphere reaches the backside. In contrast, the sky view factor at the HSAT’s backside POA changes continuously with sun position. In the morning and afternoon, the backside has a maximum sky view factor of 0.2 when the tilt is 60°. Midday, the sky view factor is reduced to zero when the tilt is horizontal. Because the sky diffuse spectrum is blue shifted on clear days (Kirn and Topic, 2017), we can expect the HSAT system to show the lowest spectral mismatch at the ends of the day when at a 60° tilt.

Fig. 10 shows daily timeseries of SMM_{Back} to illustrate the dependency of backside spectral shifts on the view factor from the sky to the array’s backside ($F_{Sky \rightarrow PV, Rear}$) and on the view factor from the ground to the array’s backside ($F_{Ground \rightarrow PV, Rear}$). Except for the snow albedo case, the data shown in Fig. 10 were recorded under clear skies. As expected, the lowest SMM_{Back} values on the HSAT occur in the morning and afternoon when $F_{Sky \rightarrow PV, Rear}$ is highest, and the highest SMM_{Back} values occur midday when $F_{Ground \rightarrow PV, Rear}$ is close to one. The daily SMM_{Back} values on the static 25° FT system do not change significantly, which follows the expected trend given the constant view factors $F_{Sky \rightarrow PV, Rear}$ and $F_{Ground \rightarrow PV, Rear}$.

Fig. 11 shows the density of SMM_{Back} values during the 15-month

measurement campaign. The wider dispersion of SMM_{Back} in the HSAT case is attributed to the constantly changing sky view factors. Fig. 12 illustrates this relationship between SMM_{Back} and sky view factor on the backside of the 2-in-portrait HSAT. Snow albedo is not shown in Fig. 12 due to a lack of measured data. The results show a strong correlation with sky view factor and reveal that the diffuse fraction (K_d) is an important secondary effect. Most measurements in Fig. 12 were recorded during very clear days (K_d less than 0.2) or very cloudy days (K_d greater than 0.9). This is because the variability index filter removed most measurements outside these conditions.

The literature contains several spectral models for monofacial PV that are based largely on correlations with air mass (Huld et al., 2009) (King et al., 2004), (Lee and Panchula, 2016), (Pelland et al., 2020). However, we found air mass to be a poor indicator of SMM_{Back} . We used a bootstrap forest model to identify the most significant predictors of SMM_{Back} from our available weather and tracker position data. We found that a simplified predictive model for SMM_{Back} should at minimum include the backside array sky view factor, and the sky diffuse fraction. The third piece of information needed is a classification of the ground surface (e.g., green grass), which could be obtained with measurements from a multifilter radiometer (see Section 3.4) or the NDVI. With simple multiple linear regression techniques, we obtained root mean squared errors (RMSE) for SMM_{Back} between 0.014 and 0.020, depending on the albedo. Although the correlations in Fig. 12 are made with results from single axis tracker simulations, the model is likely to apply to systems with different azimuth orientations when the diffuse light received by the backside is only isotropic diffuse. This would include multi-row equator facing FT systems with several rows behind the array that block the horizon brightening component.

Fig. 10, Fig. 11 and Fig. 12 show that the $G_{POA, rear, \lambda}$ spectral

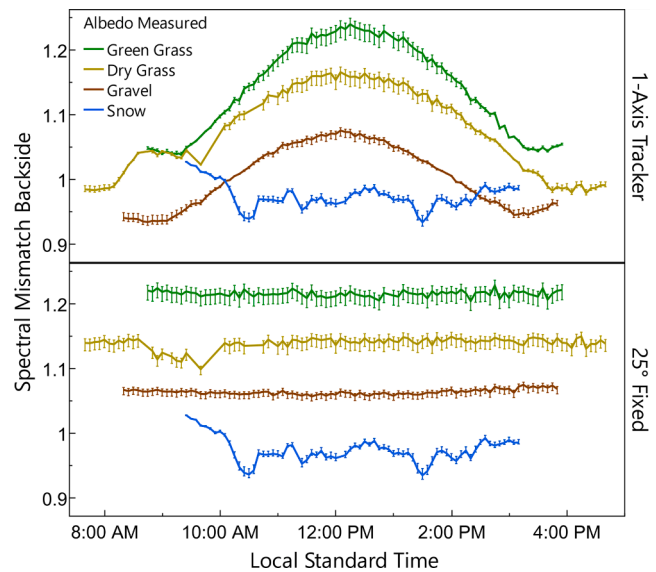


Fig. 10. Backside spectral mismatch on select days for the single axis tracker (top) and fixed-tilt systems (bottom). The raw spectral albedo recorded these days is shown in Fig. 6 and Fig. 8. The error bars around each timeseries show the range of spectral mismatch values of three different bifacial cell concepts.

Table 2

Backside spectral impacts of Si bifacial devices mounted on two structure types above four ground surfaces. The results are the average spectral impacts of bifacial IBC, n-PERT and PERC concepts.

Structure	Green Grass			Dry Grass			Gravel			Snow		
	SI_{Back} Mean	SI_{Back} Range	N	SI_{Back} Mean	SI_{Back} Range	N	SI_{Back} Mean	SI_{Back} Range	N	SI_{Back} Mean	SI_{Back} Range	N
1A Tracker	1.133	0.012	15,648	1.093	0.010	18,792	1.007	0.000	28,698	0.981	0.007	810
25° Fixed	1.196	0.022	15,648	1.155	0.019	18,792	1.046	0.007	28,698	0.980	0.007	810

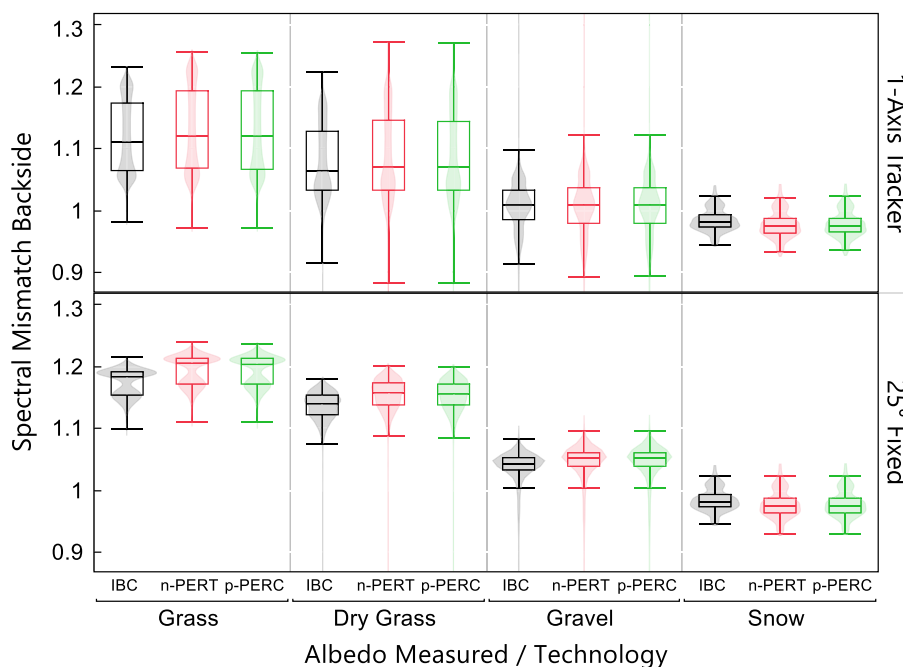


Fig. 11. Box and whisker plots of backside spectral mismatch for single axis tracker (top) and fixed-tilt systems (bottom). The x-axis levels are bifacial cell technology within albedo. The shaded violin plots show the density of spectral mismatch values.

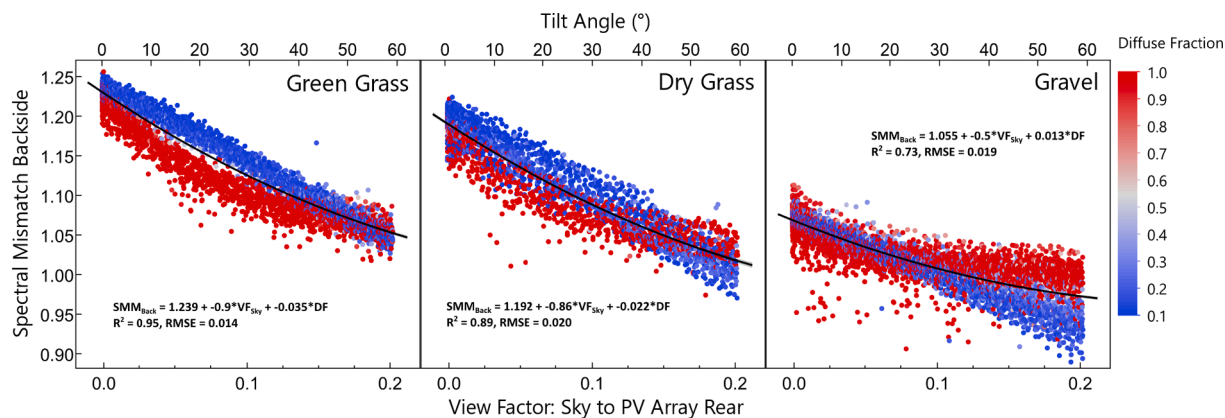


Fig. 12. Backside spectral mismatch of PERC versus sky view factor for three measured albedo conditions: green grass (left), dry grass (center) and gravel (right). The tilt angle of the 2-in-portrait tracker system is shown on the secondary x-axis above. (For interpretation of the references to colour in this figure legend, the reader is referred to the web version of this article.)

distribution deviates significantly from AM1.5G over daily and seasonal timescales. Indeed, backside spectral gains as high as 25% occur with green grass albedo, but since rear irradiance makes up only 5–15% of total irradiance, such backside spectral gains are reduced to approximately 2% in most conditions. A complementary reference spectrum for backside bifacial PV characterization (i.e., an AM1.5R) could conceivably reduce spectral errors observed in the field. However, (Monokroussos et al., 2020) concluded that the industry-wide complications that would occur after introducing a new standardized spectrum are not worth the reduced spectral errors that can be achieved. Although this reason has not prevented other authors from proposing supplemental spectra to counter the shortcomings of AM1.5G (Jessen et al., 2018) (Kinsey, 2021) (Looney et al., 2020) (Myers et al., 2004), the AM1.5G spectrum is likely to remain the standard for backside bifacial PV characterizations in years to come. The question then becomes, what are the alternatives to reduce the spectral uncertainties encountered in fielded bifacial systems?

Backside spectral mismatch can be minimized using a rear facing

reference cell that has a similar spectral responsivity as the backside of the bifacial cells within the array. However, the standardization of such a cell's position within the array is still ongoing and no recommendation has yet been offered in international standards (Gostein et al., 2021). Designers of bifacial PV monitoring systems must presently understand many nuanced effects of rear POA irradiance to optimally select the number and mounting location of reference cells. The nonuniformity of $G_{POA, rear, \lambda}$ is one such effect that is infrequently considered, but can be significant in some cases, as illustrated in Fig. 13.

Fig. 13 shows SMM_{Back} of the PERC device discretized in 20 equally spaced segments, which correspond roughly to the 20 cell locations on the 2-in-portrait HSAT and FT systems. The simulations use spectral data from a cloudless day during the green grass albedo period (25.03.2020). In the HSAT simulation, segment 1 is the western most cell and segment 20 is the eastern most cell. In the FT simulation, segment 1 corresponds to the topmost cell and segment 20 corresponds to the bottom most cell.

The results indicate that a single backward facing reference cell is not likely to represent the effective rear irradiance on an HSAT system

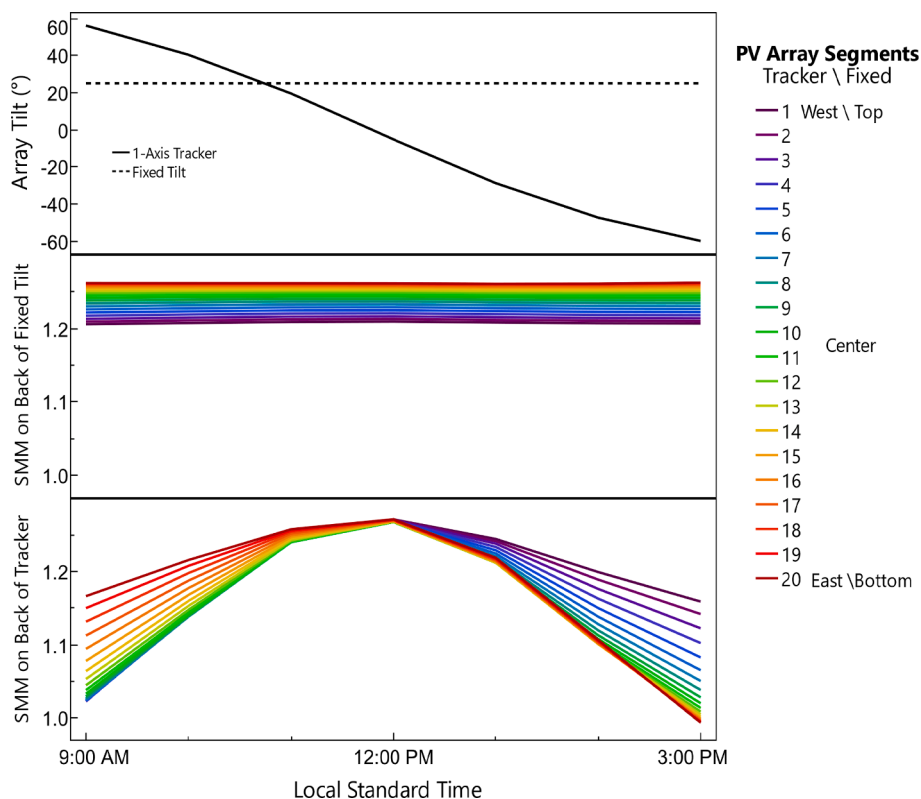


Fig. 13. Simulated nonuniformity of backside spectral mismatch of PERC using spectral albedo measurements of green grass on a clear day near the spring equinox. The two cases shown are 2-in-portrait tracked (bottom figure) and fixed-tilt systems (center figure). (For interpretation of the references to colour in this figure legend, the reader is referred to the web version of this article.)

because SMM_{Back} within the array varies by as much as ± 0.075 (7.5%) in the morning and afternoon. In the morning when the tracker is pointing east, segment 1 (west) is highest in the sky and segment 20 (east) is lowest to the ground. Thus, segment 1 receives the largest contribution of sky diffuse irradiance—resulting in the lowest SMM_{Back} —and segment 20 has the largest contribution of ground reflected irradiance resulting in the largest SMM_{Back} . Midday when the tracker is horizontal, the ground view factor of all 20 segments is unity, and there is no SMM gradient at solar noon.

The dispersion of SMM_{Back} within the 2-in-portrait FT array is about ± 0.03 (3%) throughout the day if the sun is in front of the array. This spectral gradient is large enough to advise two backward facing reference cells – one for the bottom and top halves of the array. The bottom cell in the 25° FT system shows spectral gains 6% higher than the top cell, a difference which is again attributed to the different exposure to sky diffuse and ground reflected light.

We conclude this section with a note on the uncertainty of spectral mismatch (SMM) and spectral impact (SI). As mentioned in Section 2.2 (Fig. 2), the measurement drift of the spectroradiometers used for GHI and DNI measurements were mostly within the uncertainty of the calibration, but the instrument used for RHI measurements drifted significantly beyond the calibration uncertainty at some wavelengths. To understand the implications of these wavelength shifts on the results, we compared SMM_{Back} calculations using calibrations from 22.01.2020 (pre-deployment) and 11.05.2021 (post-deployment). The results showed that SMM_{Back} agreed within 0.004 (0.4%) or better 99% of the time, given the two sets of calibration coefficients and the albedo and sky conditions observed during the test period. The small difference in SMM_{Back} is because the wavelength shifts did not significantly affect the area under the measured spectral albedo curves. Finally, uncertainty of SI can be inferred from the work of (Dirnberger et al., 2015a), who used spectroradiometers from the same manufacturer as used in this work and concluded that the minimum standard uncertainty is 0.009 (0.9%)

for monofacial single junction c-Si SI calculations.

3.4. Impact of wavelength sampling reduction on spectral mismatch

Spectral albedo curves are not highly structured like the sun’s spectrum as was demonstrated in Fig. 6 and Fig. 8, as well as by others (Vignola et al., 2017). The 0.4 nm wavelength resolution of the spectroradiometers used in this work therefore resulted in oversampling of the spectral albedo. The benefit of the high-resolution spectral albedo setup, however, is that down sampling can be conducted to identify when spectral mismatch, or other spectral factors, show large discrepancies relative to those calculated with the high-resolution data. To this end, we truncated the 2048-pixel measurements down to 2–8 wavelength channels and repeated the SMM_{Back} calculations. Table 3 shows the different wavelength bands tested. In all these cases, the down sampled albedo spectra use the 7 nm full-width half maximum optical resolution of the MS-711 spectroradiometer. The spectral albedo between narrow band channels is interpolated with a first order spline fit. Values outside the wavelength ranges shown in Table 3 are extrapolated, with the condition that 0.001 and 1.0 are the minimum and maximum

Table 3
Summary of wavelength channels used in the different down sampling tests of the high-resolution spectral albedo measurements. A 7 nm full width half maximum resolution was used in all scenarios.

N Channels	Center wavelengths (nm)
2	500, 940
3	500, 870, 940
4	415, 615, 870, 940
5	469, 555, 645, 858, 1050
6	415, 500, 615, 673, 870, 940
7	415, 500, 615, 673, 870, 940, 1050
8	415, 555, 615, 673, 762, 870, 940, 1050

spectral albedo values allowed.

The first four wavelength channels in the five-channel scenario (469 nm, 555 nm, 645 nm, and 858 nm) are the center wavelengths of the first four bands of the MODIS satellite (Schaaf and Wang, 2015); because the fifth MODIS spectral band (1240 nm) is beyond the spectral responsivity of Si, the fifth wavelength channel used here is 1050 nm. The wavelength channels in all other scenarios are selected for their common use in multi-filter radiometer (MFR) applications (Michalsky and Hodges, 2013) (Vladutescu et al., 2013) and because they are similar to those used by (Tatsiankou et al., 2016). The six-channel case uses the same six channels as used in the works of (Michalsky and Hodges, 2013) and (Vladutescu et al., 2013). To select the wavelengths of the two, three and four-channel cases, we down sampled all possible combinations of the six-channel case and identified the combination of wavelengths, for each case, that resulted in the lowest root mean square error (RMSE) across the four measured albedo conditions. The seven-channel case simply adds an NIR channel (1050 nm) to the six-channel case, and the eight-channel case has additional measurements at 555 nm and 762 nm,

which are intended to capture the features of green vegetation. Fig. 14 shows examples of spectral albedo curves down sampled according to Table 3 for the four albedo conditions measured onsite.

Fig. 15 shows selected daily timeseries of SMM_{Back} calculated with the seven down sampling cases and with the high-resolution spectral albedo measurements. Table 4 summarizes the SMM_{Back} deviations across the entire 15-month measurement campaign in terms of the mean bias error (MBE) and RMSE.

The results indicate that SMM_{Back} can be reasonably approximated using spectral albedo measurements with just 4–8 narrow band channels. The two and three-channel down sampled cases show notably higher errors, especially in green grass and gravel albedo conditions. Given that many PV parks globally are constructed at sites where the spectral albedo is comparable to the green grass and gravel albedo conditions measured here, our down sampled SMM_{Back} results indicate that four narrow band channels is likely the bare minimum to monitor spectral albedo in bifacial PV applications. However, it is apparent in the four-channel curve of Fig. 14a that the down sampling overestimates the

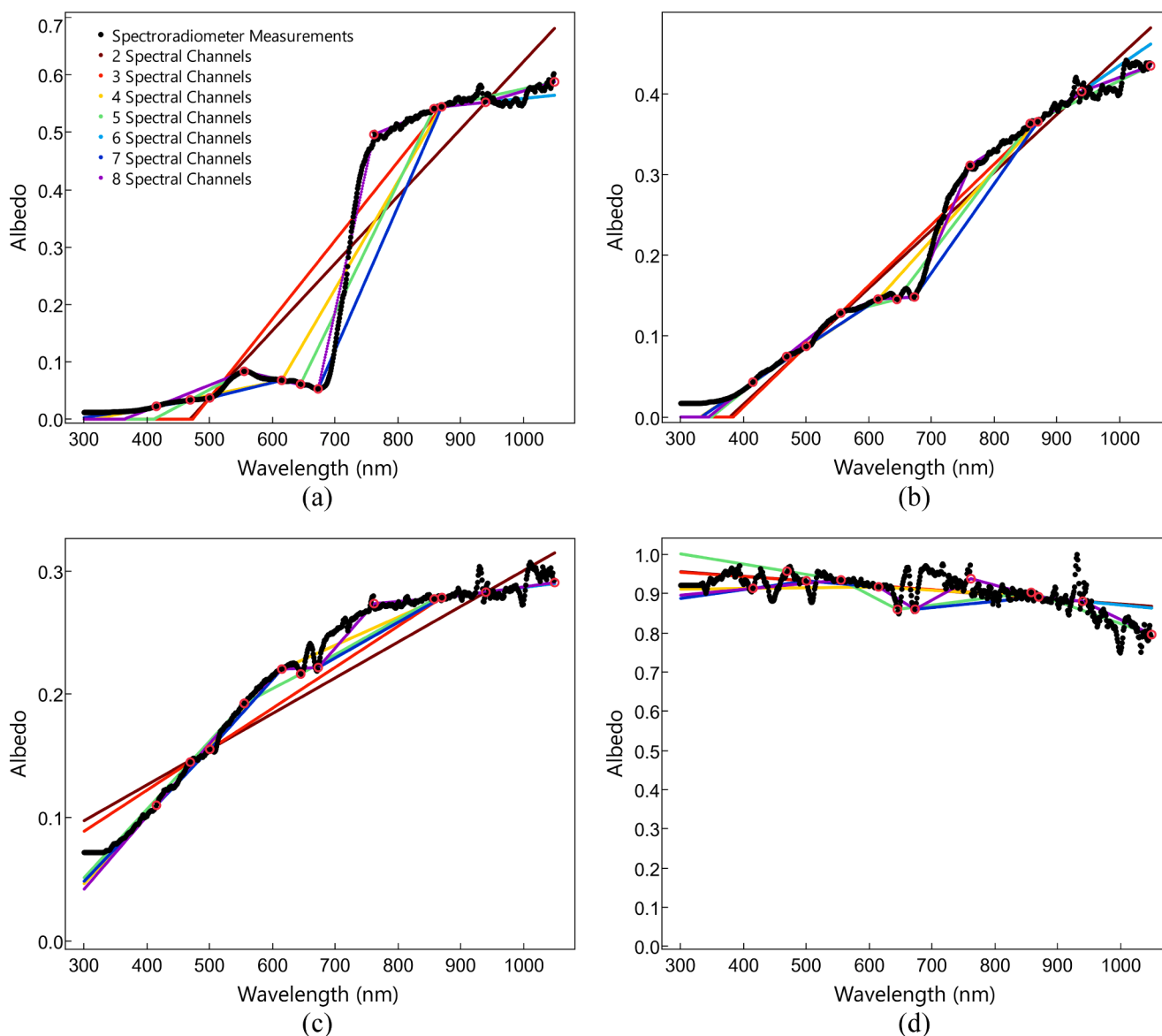


Fig. 14. Comparisons of measured and down sampled spectral albedo during the four albedo conditions: (a) green grass, (b) dry grass, (c) gravel and (d) snow. The example curves shown here are taken at 12:00 noon on the days shown in Fig. 6 and Fig. 8. The red circles correspond to the channels shown in Table 3. The red circles highlight the wavelengths at which the down sampled curves are created from the high-resolution measurements. (For interpretation of the references to colour in this figure legend, the reader is referred to the web version of this article.)

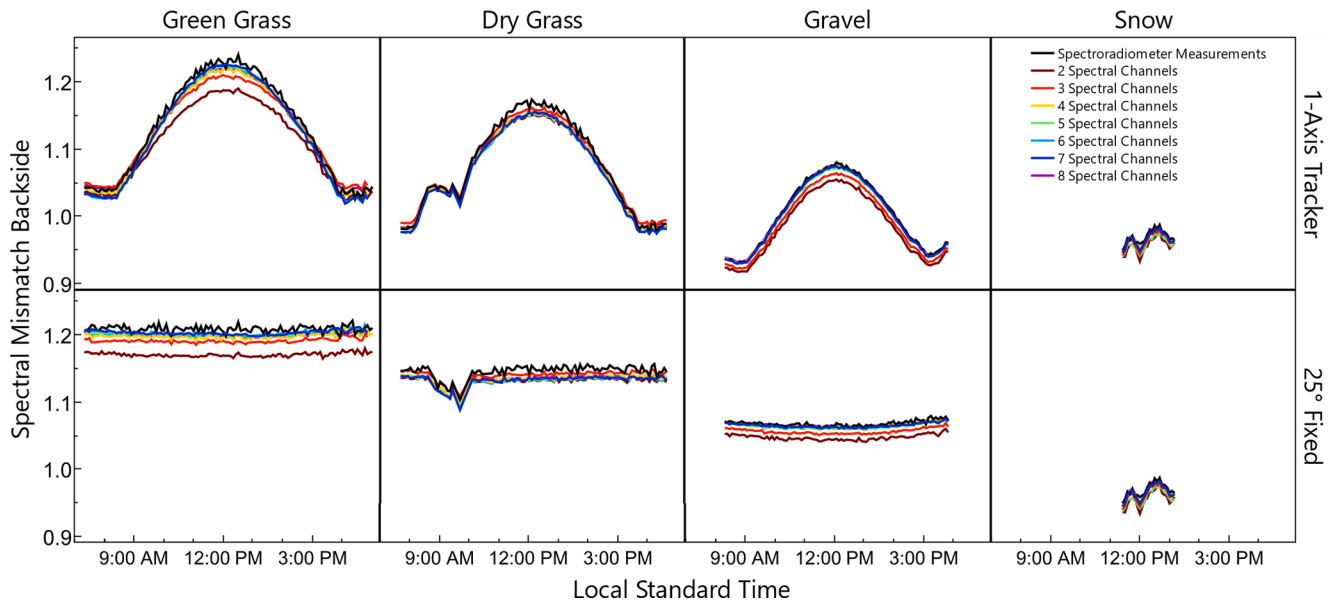


Fig. 15. Backside spectral mismatch of the PERC cell calculated with down sampled spectral albedos and high-resolution measurements. The down sampled calculations are made with the 2–8 narrow band channels shown in Table 4. Backside spectral mismatch is shown for a single axis tracker (top row) and a fixed-tilt system (bottom row). The four measured albedo conditions are displayed column-wise.

Table 4
Error Summary for backside spectral mismatch calculations performed using down sampled spectral albedo.

Structure	N Spectral Channels	Green Grass		Dry Grass		Gravel		Snow	
		MBE	RMSE	MBE	RMSE	MBE	RMSE	MBE	RMSE
1-Axis Tracker	2	-0.0243	0.0297	-0.0139	0.0175	-0.0116	0.0138	-0.0108	0.0122
	3	-0.0080	0.0170	-0.0011	0.0083	-0.0042	0.0072	-0.0056	0.0065
	4	-0.0081	0.0155	-0.0070	0.0097	0.0020	0.0038	-0.0012	0.0029
	5	-0.0056	0.0137	-0.0059	0.0083	-0.0004	0.0052	-0.0104	0.0108
	6	-0.0086	0.0155	-0.0098	0.0114	0.0004	0.0033	-0.0032	0.0042
	7	-0.0082	0.0153	-0.0095	0.0111	-0.0005	0.0035	-0.0030	0.0041
	8	-0.0060	0.0146	-0.0065	0.0098	0.0021	0.0042	-0.0006	0.0035
	25° Fixed Tilt	2	-0.0310	0.0329	-0.0199	0.0213	-0.0138	0.0156	-0.0114
3		-0.0124	0.0161	-0.0048	0.0086	-0.0049	0.0079	-0.0059	0.0068
4		-0.0097	0.0135	-0.0094	0.0115	0.0021	0.0042	-0.0013	0.0030
5		-0.0064	0.0108	-0.0075	0.0097	-0.0005	0.0058	-0.0109	0.0113
6		-0.0082	0.0125	-0.0103	0.0123	0.0003	0.0037	-0.0034	0.0043
7		-0.0077	0.0123	-0.0099	0.0120	-0.0008	0.0040	-0.0032	0.0043
8		-0.0081	0.0122	-0.0094	0.0115	0.0022	0.0046	-0.0007	0.0035

spectral albedo in some areas and underestimates it in others. Because the SMM calculation is an integrated quantity, it is possible that in cases where the down sampled spectral albedo curves show both high and low biases relative to the ground truth, the differences are effectively cancelled when assessed via the SMM factor. A more robust solution would therefore aim to recreate the spectral albedo curve across the various albedo conditions, which the eight-channel scenario (Fig. 14) does reasonably well.

Nearly all scenarios in Table 4 result in negative MBE relative to the high-resolution measurements, the exception is gravel albedo for which three of the seven scenarios show positive MBE. The RMSE of SMM_{Back} is between 0.0033 and 0.0329 with a trend toward higher errors at lower spectral resolution. The eight-channel case, however, does not always show the lowest RMSE. In fact, the RMSE of the eight-channel case and the 3–7 channel cases are within 0.005 of each other in all albedo conditions except snow. The two-channel case always shows the highest RMSE, with a maximum of 0.0329 (green grass) and a minimum of 0.0122 (snow). Since the two-channel case contains one measurement in the VIS and one in the NIR region, the errors shown in Table 4 coincide with those of Section 3.3 where it was shown that the NDVI can be used to approximate SMM_{Back} with an accuracy of ± 0.04 .

4. Conclusions

We have demonstrated that backside spectral mismatch in bifacial PV systems is dynamic on daily and seasonal timescales, and we have quantified the extent to which it is dependent on the albedo, sky conditions, and mounting structure. On clear sky days, we observed that spectrally induced performance gains peak at mid-day wherein the backside spectral gains were 25%, 15%, and 5% for green vegetation, dry vegetation, and gravel, respectively. Backside spectral effects are significantly lower on tracked versus fixed-tilt bifacial systems because of the larger sky view factors on the array backside. On clear days, when the tracker is tilted at 60° from a horizontal, the spectral effects are reduced to 5%, 0%, and -5% for green vegetation, dry vegetation, and gravel, respectively.

With the variety of albedo conditions tested here, we showed that the normalized difference vegetation index (NDVI) is a reasonable data source to estimate backside spectral effects in bifacial PV systems. Specifically, the strong correlation between SMM_{Back} and NDVI suggests that satellite derived NDVI products could be a simple method to estimate backside spectral effects. However, the small area of our test site in comparison to the pixel resolution of satellite images prevented further

examination of this conclusion.

Our 2D view factor simulations of incident backside spectrum discretized at the cell-level showed that backside POA spectral gradients (up to $\pm 7.5\%$ in the tracked case) make multiple reference cells in the same array advisable, especially in 2-in-portrait configurations. Finally, we demonstrated that high-resolution spectral albedo measurements are neither practical nor necessary for bifacial PV performance monitoring applications. When SMM_{Back} was calculated with 2 to 8 wavelengths that were judiciously sampled between 300 and 1100 nm, we demonstrated that SMM_{Back} values calculated with just 4 wavelength channels are comparable to those calculated with the full spectroradiometer measurements with $RMSE \leq 0.0155$. However, 8 spectral channels are recommended for users who are interested in recreating the spectral albedo curves as closely as possible.

Declaration of Competing Interest

The authors declare that they have no known competing financial interests or personal relationships that could have appeared to influence the work reported in this paper.

Acknowledgements

We thank Dennis Corell of DTU for supporting the spectrometer calibration efforts, Rasmus Nielsen of DTU for supporting the spectral responsivity measurements, and Dr. Joris Libal of ISC Konstanz for providing us with bifacial n-PERT and IBC cell samples.

Funding

This work was funded by the Danish Energy Technology Development and Demonstration Program (EUDP) under project contract 64018-0624.

References

- Alonso-Abella, M., Chenlo, F., Nofuentes, G., Torres-Ramírez, M., 2014. Analysis of spectral effects on the energy yield of different PV (photovoltaic) technologies: The case of four specific sites. *Energy* 67, 435–443.
- Andrews, R.W., Pearce, J.M., 2013. The Effect of Spectral Albedo on Amorphous Silicon and Crystalline Silicon Solar Photovoltaic Device Performance. *Sol. Energy* 91, 233–241.
- Anoma, M., et al., 2017. View Factor Model and Validation for Bifacial PV and Diffuse Shade on Single-Axis Trackers. Washington D.C, s.n.
- Asgharzadeh, A., Marion, B., Deline, C., Hansen, C., Stein, J.S., Toor, F., 2018. A Sensitivity Study of the Impact of Installation Parameters and System Configuration on the Performance of Bifacial PV Arrays. *IEEE J. Photovoltaics* 8 (3), 798–805.
- Baldrige, A.M., Hook, S.J., Grove, C.I., Rivera, G., 2009. The ASTER spectral library version 2.0. *Remotes Sens Environ.* 113 (4), 711–715.
- Belluardo, G., Galleano, R., Zaïman, W., Pravettoni, M., Halwachs, M., Fucci, R., Drobisch, A., Friederichs, M., Haverkamp, E., Phinikarides, A., Friesen, G., 2018. Are the spectroradiometers used by the PV community ready to accurately measure the classification of solar simulators in a broader wavelength range? *Sol. Energy* 173, 558–565.
- Berrian, D., Libal, J., 2020. A comparison of ray tracing and view factor simulations of locally resolved rear irradiance with the experimental values. *Prog. Photovolt.* 28 (6), 609–620.
- Berrian, D., 2020. Accuracy of Ray Tracing and View Factor Optical Models - PhD Dissertation. Albert-Ludwigs-University, Freiburg im Breisgau, Germany.
- Blakesley, J.C., et al., 2020. Effective spectral albedo from satellite data for bifacial gain calculations of PV systems. *Virtual, s.n.*
- Brennan, M.P., Abramase, A.L., Andrews, R.W., Pearce, J.M., 2014. Effects of spectral albedo on solar photovoltaic devices. *Sol. Energy Mater. Sol. Cells* 124, 111–116.
- Chiodetti, M. et al., 2016. *PV Bifacial Yield Simulation with a Variable Albedo Model*. Munich, s.n.
- Chudinow, D., Haas, J., Díaz-Ferrán, G., Moreno-Leiva, S., Eltrop, L., 2019. Simulating the energy yield of a bifacial photovoltaic power plant. *Sol. Energy* 183, 812–822.
- Chudinow, D., Klenk, M., Eltrop, L., 2020. Impact of field design and location on the techno-economic performance of fixed-tilt and single-axis tracked bifacial photovoltaic power plants. *Sol. Energy* 207, 564–578.
- Coakley, J.A., 2003. Reflectance and Albedo, Surface. In: *Encyclopedia of Atmospheric Sciences*. Elsevier, pp. 1914–1923, 10.1016/B0-12-227090-8/00069-5.
- Deline, C. & Pelaez, S., 2017. *Bifacial Radiance*. *Computer Software*. [Online] Available at: https://github.com/NREL/bifacial_radiance.
- Deline, C., Ayala Pelaez, S., MacAlpine, S., Olalla, C., 2020. Estimating and parameterizing mismatch power loss in bifacial photovoltaic systems. *Progress in Photovoltaics* 28 (7), 691–703.
- Dirnberger, D., Müller, B., Reise, C., 2015a. On the uncertainty of energetic impact on the yield of different PV technologies due to varying spectral irradiance. *Sol. Energy* 111, 82–96.
- Dirnberger, D., Blackburn, G., Müller, B., Reise, C., 2015b. On the impact of solar spectral irradiance on the yield of different PV technologies. *Sol. Energy Mater. Sol. Cells* 132, 431–442.
- Dittmann, S. et al., 2019. Comparative Analysis of Albedo Measurements at Multiple Sites Worldwide. Marseille, s.n.
- Dullweber, T., et al., 2016. PERC+: industrial PERC solar cells with rear Al grid enabling bifaciality and reduced Al paste consumption. *Progress in Photovoltaics* 24, 1487–1498.
- Dullweber, T., Schmidt, J., 2016. Industrial Silicon Solar Cells Applying the Passivated Emitter and Rear Cell (PERC) Concept—A Review. *IEEE J. Photovoltaics* 6 (5), 1366–1378.
- Dupre, O., et al., 2020. Design Rules to Fully Benefit From Bifaciality in Two-Terminal Perovskite/Silicon Tandem Solar Cells. *IEEE J. Photovoltaics* 714–721.
- Dye, D., Tucker, C., 2003. Seasonality and trends of snow-cover, vegetation index, and temperature in northern Eurasia. *Geophys. Res. Lett.* 30 (7), 58–61.
- Ernst, M., Holst, H., Winter, M., Altermatt, P., 2016. SunCalculator: A program to calculate the angular and spectral distribution of direct and diffuse solar radiation. *Sol. Energy Mater. Sol. Cells* 157, 913–922.
- European Space Agency, 2021. *Sentinel VGT S NDVI*. [Online] Available at: <https://sentinel.esa.int/web/sentinel/technical-guides/sentinel-3-synergy/vgt-s-ndvi> [Accessed 30 6 2021].
- Galleano, R. et al., 2019. *Spectroradiometer Comparison under Outdoor Direct Normal Irradiance and Indoor High-Power AMO-Like Conditions*. Marseille, France, 36th European Photovoltaic Solar Energy Conference and Exhibition.
- Gates, D., Keegan, H., Schleter, J., Weidner, V., 1965. Spectral Properties of Plants. *Appl. Opt.* 4, 11–20.
- Gostein, M., et al., 2021. Measuring Irradiance for Bifacial PV Systems. *Virtual48th IEEE Photovoltaic Specialists Conference*.
- Gostein, M., Marion, B., Stueve, B., 2020. Spectral Effects in Albedo and Rearside Irradiance Measurement for Bifacial Performance Estimation. *Virtual, s.n.*
- Green, M., 2015. The Passivated Emitter and Rear Cell (PERC): From conception to mass production. *Sol. Energy* 143, 190–197.
- Gueymard, C., 1995. *SMARTS2, A Simple Model of the Atmospheric Radiative Transfer of Sunshine: Algorithms and performance assessment Authors*, s.l.: Florida Solar Energy Center Report (FSEC-PF-270-95).
- Guo, S., Walsh, T., Peters, M., 2013. Vertically mounted bifacial photovoltaic modules: A global analysis. *Energy* 61, 447–454.
- Hezel, R., 2003. Novel Applications of Bifacial Solar Cells. *Prog. Photovoltaics* 11, 549–556.
- Hohl-Ebinger, J., Warta, W., 2011. Uncertainty of the spectral mismatch correction factor in STC measurements on photovoltaic devices. *Prog. Photovolt.* 19.
- Huang, S., et al., 2020. A commentary review on the use of normalized difference vegetation index (NDVI) in the era of popular remote sensing. *J. For. Res.* 32 (5), 1–6.
- Huld, T., Sample, T. & Dunlop, E., 2009. *A simple model for estimate the influence of spectrum variations on PV performance*. Hamburg, 24th EUPVSEC.
- International Electrotechnical Commission, 2019a. *IEC 60904-3 Ed. 4.0*, s.l.: s.n.
- International Electrotechnical Commission, 2019b. *IEC 60904-7 Ed. 4.0*, s.l.: s.n.
- Iqbal, M., 1983. Chapter 9: Ground Albedo. In: *An Introduction to Solar Radiation*. Academic Press, New York and London, pp. 281–293.
- Ishii, T., Otani, K., Itagaki, A., Utsunomiya, K., 2013. A simplified methodology for estimating solar spectral influence on photovoltaic energy yield using average photon energy. *Energy Science and Engineering*.
- Jessen, W., et al., 2018. Proposal and evaluation of subordinate standard solar irradiance spectra for applications in solar energy systems. *Sol. Energy* 168, 30–43.
- King, D., Boyson, B. & Kratochvill, J., 2004. *Photovoltaic Array Performance Model*, s.l.: Sandia Report (SAND2004-3535).
- Kinsey, G., 2021. Solar cell efficiency divergence due to operating spectrum variation. *Sol. Energy* 217, 49–57.
- Kirn, B., Topic, M., 2017. Diffuse and direct light solar spectra modeling in PV module performance rating. *Sol. Energy* 150, 310–316.
- Kondratiev, K. Y., Mironova, Z. F. & Otto, A. N., 1964. Spectral albedo of natural surfaces. *pure and applied geophysics*, Volume 59, p. 207–216.
- Kondratyev, K., 1969. Section 7.1: Spectral Albedo of Natural Underlying Surfaces. In: *Radiation in the Atmosphere*. Academic Press, New York and London, pp. 411–422.
- Kopecek, R., Libal, J., 2021. Bifacial Photovoltaics 2021: Status, Opportunities and Challenges. *Energies* 14 (2076).
- Kopecek, R. et al., 2020. *ZEBRA technology: low cost bifacial IBC solar cells in mass production with efficiency exceeding 23.5%*. Calgary, s.n.
- Korevaar, M., et al., 2020. Simulation and Validation of Bifacial Irradiance Sensor Mounting Position. *Virtual Meeting, 37th European Solar Energy Conference (EUPVSEC)*.
- Krinov, E., 1953. *Spectral reflectance properties of natural formations*. Technical translation TT-439 by E. Belkov, National Research Council of Canada, Ottawa ed. USSR: Area Methods Laboratory, Academy of Sciences (originally in Russian, 1947).
- Lamers, M., et al., 2018. Temperature effects of bifacial modules: Hotter or cooler? *Sol. Energy Mater. Sol. Cells* 185, 192–197.
- Ledesma, J., et al., 2020. A simulation model of the irradiation and energy yield of large bifacial photovoltaic plants. *Sol. Energy* 206, 522–538.

- Lee, M. & Panchula, A., 2016. *Spectral correction for photovoltaic module performance based on air mass and precipitable water*. Portland, OR, 43rd IEEE Photovoltaic Specialists Conference.
- Looney, E., et al., 2020. Representative identification of spectra and environments (RISE) using k-means. *Prog. Photovolt.* 29, 200–211.
- Lossen, J. et al., 2015. *From Lab to Fab: Bifacial n-Type Cells Entering Industrial Production*. Hamburg, Germany, Proceedings of the 31st European Photovoltaic Solar Energy Conference and Exhibition.
- Marion, B., 2021. Measured and satellite-derived albedo data for estimating bifacial photovoltaic system performance. *Sol. Energy* 215, 321–327.
- McIntosh, K., Abbott, M., Sudbury, B., Meydray, J., 2019. Mismatch Loss in Bifacial Modules Due to Nonuniform Illumination in 1-D Tracking Systems. *IEEE J. Photovoltaics* 9 (6), 1504–1512.
- McIntosh, K., et al., 2020. Irradiance on the upper and lower modules of a two-high bifacial tracking system. Virtual Meeting, 47th IEEE Photovoltaics Specialist Conference (PVSC).
- Mekemeche, A., Beghdad, M., 2020. Impact of the Environmental Effective Albedo on the Performance of PERC + Solar Cells. *Silicon* 29.
- Michalsky, J., Hodges, G., 2013. Field Measured Spectral Albedo-Four Years of Data from the Western U.S. Prairie. *J. Geophys. Res. Atmospheres* 118, 813–825.
- Minnis, P., Mayor, S., Smith, W., Young, D., 1997. Asymmetry in the Diurnal Variation of Surface Albedo. *IEEE Trans. Geosci. Remote Sens.* 35 (4), 879–890.
- Monokroussos, C., et al., 2020. Rear-side spectral irradiance at 1 sun and application to bifacial module power rating. *Prog. Photovolt.*
- Myers, D., Emery, K., Gueymard, C., 2004. Revising and Validating Spectral Irradiance Reference Standards for Photovoltaic Performance Evaluation. *J. Sol. Energy Eng.* 126, 567–574.
- Myers, D. R., 2011. Quantitative analysis of spectral impacts on silicon photodiode radiometers. *40th ASES National Solar Conference 2011, SOLAR 2011*, 1(April), pp. 97–102.
- NASA, 2021. *MODIS Vegetation Index Products*. [Online] Available at: <https://modis.gsfc.nasa.gov/data/dataproduct/mod13.php>.
- Nofuentes, G., et al., 2017. Is the average photon energy a unique characteristic of the spectral distribution of global irradiance? *Sol. Energy* 149, 32–43.
- Nordmann, T., Vontobel, T. & Clavadetscher, L., 2012. 15 Years of Practical Experience in Development and Improvement of Bifacial Photovoltaic Noise Barriers Along Highways and Railway Lines in Switzerland. Frankfurt, Germany, 27th European Photovoltaic Solar Energy Conference and Exhibition.
- Pal, S., Reinders, A., Saive, R., 2020. Simulation of Bifacial and Monofacial Silicon Solar Cell Short-Circuit Current Density Under Measured Spectro-Angular Solar Irradiance. *IEEE J. Photovoltaics* 10 (6), 1803–1815.
- Pelaez, S.A., et al., 2019a. Model and Validation of Single-Axis Tracking with Bifacial PV. *IEEE J. Photovoltaics* 9 (3), 715–721.
- Pelaez, S., et al., 2019b. Comparison of Bifacial Solar Irradiance Model Predictions With Field Validation. *IEEE J. Photovoltaics* 9 (1), 82–88.
- Pelland, S. et al., 2020. *Development and Testing of the PVSPEC Model of Photovoltaic Spectral Mismatch Factor*. Calgary, Canada, 47th IEEE Photovoltaic Specialists Conference.
- Polo, J., Alonso-Abella, M., Ruiz-Arias, J., Balanzategui, J., 2017. Worldwide analysis of spectral factors for seven photovoltaic technologies. *Sol. Energy* 142, 194–203.
- Pravettoni, M., et al., 2018. Spectroradiometry in PV: how inter-laboratory comparison may improve measurement accuracy. Waikaloa, Hawaii, 7th World Conference on Photovoltaic Energy Conversion.
- Riedel-Lyngskær, N., et al., 2020a. A Spatial Irradiance Map Measured on the Rear Side of a Utility-Scale Horizontal Single Axis Tracker with Validation using Open Source Tools. Virtual Meeting, 47th IEEE Photovoltaics Specialist Conference (PVSC).
- Riedel-Lyngskær, N., et al., 2020b. Validation of Bifacial Photovoltaic Simulation Software against Monitoring Data from Large-Scale Single Axis Trackers and Fixed Tilt Systems in Denmark. *Applied Sciences* 10 (23), 1–29.
- Riedel-Lyngskær, N., et al., 2021. Spectral Albedo in Bifacial Photovoltaic Modelling: What can be Learned from Onsite Measurements? Miami, FL, 48th IEEE Photovoltaic Specialists Conference.
- Riedel, N., et al., 2018. Direct Beam and Diffuse Spectral Irradiance Measurements in a Nordic Country Analyzed With the Average Photon Energy Parameter. Waikoloa, United States, s.n.
- Ripalda, J., Chemisana, D., Llorens, J. & Garcia, I., 2020. Location-Specific Spectral and Thermal Effects in Tracking and Fixed Tilt Photovoltaic Systems. *iScience*, 23 (101634).
- Rodriguez-Gallegos, C., et al., 2020. Global Techno-Economic Performance of Bifacial and Tracking Photovoltaic Systems. *Joule* 4, 1514–1541.
- Rossa, C., Martinez-Moreno, F., Lorenzo, E., 2021. Experimental observations in mismatch losses in monofacial and bifacial PV generators. *Progress Photovolt.*
- Rouse, J., Haas, R., Scheel, J. & Deering, D., 1974. *Monitoring Vegetation Systems in the Great Plains with ERTS*. s.l., s.n., pp. 48–62.
- Russel, T.C.R., et al., 2017. The Influence of Spectral Albedo on Bifacial Solar Cells: A Theoretical and Experimental Study. *IEEE J. Photovolt.* 7 (6), 1611–1619.
- Schaaf, C., Wang, Z., 2015. MCD43A3 MODIS. [Online].
- Schinke, C., Pollex, H., Winter, S., 2020. Calibrating spectrometers for measurements of the spectral irradiance caused by solar radiation. *Metrologia*.
- Stein, J., Hansen, C. & Reno, M., 2012. *The Variability Index: A New and Novel Metric for Quantifying Irradiance and PV Output Variability*. s.l.: Sandia Report: SAND2012-2088C.
- Stueve, B., 2019. *Field Albedo Measurements*. Amsterdam, biflPV Workshop.
- Sun, X., Khan, M., Deline, C., Alam, M., 2018. Optimization and performance of bifacial solar modules: A global perspective. *Appl. Energy* 212, 1601–1610.
- Tatsiankou, V., et al., 2016. Design principles and field performance of a solar spectral irradiance meter. *Sol. Energy* 133, 94–102.
- Tuomiranta, A. et al., 2020. *Comparative Field Performance Assessment of Bifacial Solar Modules*. Calgary, 7th IEEE Photovoltaic Specialists Conference (PVSC), p. 1033–1034.
- VDMA, 2021. *International Technology Roadmap for Photovoltaics (ITRPV): Twelfth Edition*, s.l.: s.n.
- Vignola, F., Michalsky, J. & Stoffel, T., 2017. Chapter 9: Albedo. In: *Solar Radiation and Infrared Radiation Measurements*. Boca Raton, FL: CRC Press, p. 193–204.
- Vladutescu, D., et al., 2013. Aerosol Transport and Source Attribution Using Sunphotometers, Models and In-Situ Chemical Composition Measurements. *IEEE Trans. Geosci. Remote Sens.* 5 (7), 3803–3811.
- Vogt, M. R. et al., 2018. Impact of using spectrally resolved ground albedo data for performance simulations of bifacial modules. Brussels, s.n.
- Wang, H., Cheng, X., Yang, H., 2020. Temperature Coefficients and Operating Temperature Verification for Passivated Emitter and Rear Cell Bifacial Silicon Solar Module. *IEEE J. Photovoltaics* 10 (3), 729–739.
- Ward, G., 1994. The RADIANCE Lighting Simulation and Rendering System. Proceedings of the 21st annual conference on Computer graphics and interactive techniques.
- Wilson, G., et al., 2020. The 2020 photovoltaic technologies roadmap. *J. Phys. D Appl. Phys.* 53 (49).
- Yusufoğlu, U., et al., 2015. Analysis of the Annual Performance of Bifacial Modules and Optimization Methods. *IEEE J. Photovoltaics* 5 (1), 320–328.
- Zhang, Y., Yu, Y., Meng, F., Liu, Z., 2020. Experimental Investigation of the Shading and Mismatch Effects on the Performance of Bifacial Photovoltaic Modules. *IEEE J. Photovoltaics* 10 (1).
- Ziar, H., Sönmez, F., Isabella, O., Zeman, M., 2019. A comprehensive albedo model for solar energy applications: Geometric spectral albedo. *Appl. Energy* 255.